The FALCON concept: multi-object adaptive optics and atmospheric tomography for integral field spectroscopy - principles and performance on an 8-m telescope

François Assémat, Éric Gendron, François Hammer

▶ **To cite this version:**

François Assémat, Éric Gendron, François Hammer. The FALCON concept: multi-object adaptive optics and atmospheric tomography for integral field spectroscopy - principles and performance on an 8-m telescope. Monthly Notices of the Royal Astronomical Society, 2007, 376, pp.287-312. 10.1111/j.1365-2966.2007.11422.x . hal-03797214

HAL Id: hal-03797214
https://hal.science/hal-03797214

Submitted on 4 Oct 2022

HAL is a multi-disciplinary open access archive for the deposit and dissemination of scientific research documents, whether they are published or not. The documents may come from teaching and research institutions in France or abroad, or from public or private research centers.

L'archive ouverte pluridisciplinaire **HAL**, est destinée au dépôt et à la diffusion de documents scientifiques de niveau recherche, publiés ou non, émanant des établissements d'enseignement et de recherche français ou étrangers, des laboratoires publics ou privés.

Mon. Not. R. Astron. Soc. **376,** 287–312 (2007) doi:10.1111/j.1365-2966.2007.11422.x

The FALCON concept: multi-object adaptive optics and atmospheric tomography for integral field spectroscopy – principles and performance on an 8-m telescope

F. Assémat,[1,2]★ E. Gendron[3]★ and F. Hammer[1]★

[1]*GEPI, Observatoire de Paris–Meudon, 92195 Meudon, France*
[2]*Physics Department, University of Durham, South Road, Durham DH1 3LE*
[3]*LESIA, Observatoire de Paris–Meudon, 92195 Meudon, France*

Accepted 2006 December 19. Received 2006 December 18; in original form 2006 April 3

ABSTRACT

Integral field spectrographs are major instruments with which to study the mechanisms involved in the formation and the evolution of early galaxies. When combined with multi-object spectroscopy, those spectrographs can behave as machines used to derive physical parameters of galaxies during their formation process. Up to now, there has been only one available spectrograph with multiple integral field units, i.e. FLAMES/GIRAFFE on the European Southern Observatory (ESO) Very Large Telescope (VLT). However, current ground-based instruments suffer from a degradation of their spatial resolution due to atmospheric turbulence. In this article we describe the performance of FALCON, an original concept of a new-generation multi-object integral field spectrograph with adaptive optics for the ESO VLT. The goal of FALCON is to combine high angular resolution (0.25 arcsec) and high spectral resolution ($R > 5000$) in the J and H bands over a wide field of view (10×10 arcmin^2) in the VLT Nasmyth focal plane. However, instead of correcting the whole field, FALCON will use multi-object adaptive optics (MOAO) to perform the adaptive optics correction locally on each scientific target. This requires us then to use atmospheric tomography in order to use suitable natural guide stars for wavefront sensing. We will show that merging MOAO and atmospheric tomography allows us to determine the internal kinematics of distant galaxies up to $z \approx 2$ with a sky coverage of 50 per cent, even for objects observed near the Galactic pole. The application of such a concept to extremely large telescopes seems therefore to be a very promising way to study galaxy evolution from $z = 1$ to redshifts as high as $z = 7$.

Key words: instrumentation: adaptive optics – instrumentation: spectrographs – methods: numerical – galaxies: high-redshift – galaxies: kinematics and dynamics.

1 INTRODUCTION

Thanks to the *Hubble Space Telescope*, astronomers have been able to determine the morphology of distant galaxies located at $z > 0.5$, showing that galaxies in the past were mostly irregular and smaller than those in the local Universe (Abraham & van den Bergh 2001; van den Bergh 2002), and had higher merging rates (Le Fèvre et al. 2000; Bundy et al. 2004). The use of spatially resolved colour maps has also allowed us to highlight regions of star formation as well as showing that galaxy cores were bluer than the bulges of today's galaxies (Abraham et al. 1999a; Zheng et al. 2004).

Spectroscopic studies have also taught us that star formation rates (SFRs) were higher in distant galaxies, in particular in luminous infrared galaxies (LIRGs) where SFRs can reach 100 $M_\odot$ yr^{-1}, and that the density of star formation was much higher at $z = 1$ than today (Madau et al. 1996; Flores et al. 1999). Therefore, when the re-emission from the dust in the infrared (IR) is taken into account, a simple integration of the global star formation history shows that half of the present-day stars have been forming since $z \approx 1$–1.5 (Dickinson et al. 2003; Hammer et al. 2005).

However, dynamical information on distant galaxies, which is crucial for their study, still is not well known. Indeed, spatially resolved colour maps allow us to show where the star formation occurs, but not to know how masses and gas are distributed in those galaxies, nor to know the physical and chemical properties of the gas. Also, the question of the evolution of the fraction of barred galaxies is still controversial today (Abraham et al. 1999b; Sheth et al. 2003; Zheng et al. 2005). Finally, the way that galaxies in merging systems were assembling their masses in the past is still mysterious, as is the influence of dark matter in those exchanges. Kinematics and

★E-mail: francois.assemat@durham.ac.uk (FA); eric.gendron@obspm.fr (EG); francois.hammer@obspm.fr (FH)

© 2007 The Authors. Journal compilation © 2007 RAS

Downloaded from https://academic.oup.com/mnras/article/376/1/287/973575 by CNRS - ISTO user on 04 October 2022

chemistry of galaxies up to $z \approx 2$ are therefore required in order to evaluate the velocity fields of their main components (bulges and discs), to determine how important are the respective roles of the merging phenomenon and the dark matter, and finally to establish the physical origin of the Hubble sequence. At these redshifts, the important features such as the Hα emission lines or the stellar absorption lines are redshifted into the near-infrared, in the *J* and *H* bands. This means that integral field spectroscopy (IFS) is required, with a high spectral resolution ($3000 \leqslant R \leqslant 15\,000$), but also with a good spatial sampling (1–2 kpc) of the velocity field, implying a spatial resolution (0.15–0.25 arcsec) better than the atmospheric seeing. Moreover, there are other important issues such as the field of view (FoV) and the multiplex capability. Indeed, it is important to observe galaxies on scales greater than the correlation length (4 to 9 Mpc), leading to a minimum FoV of 100 arcmin^2. Observations of several cosmological fields will then allow us not to be sensitive to cosmic variance effects, and a multiplex capability is then required so that several objects can be observed simultaneously, providing a gain in exposure time.

In order to reach the required image quality, the solution is to use adaptive optics (AO) (Roddier 1999). AO allows us to compensate in real-time for the distortion of the wavefront caused by the turbulence in the Earth's atmosphere, providing to the telescopes their nominal angular resolution (diffraction-limited imaging). However, the FoV on which this resolution is achieved is very low. Indeed, all the AO systems built before now work with the *classical* AO method, where a guide star (natural or artificial), bright enough and close enough to the science target, is used to measure the incoming turbulent wavefront properly and compensate for it. In these conditions, the compensated FoV around the guide star is equal to a few times the isoplanatic patch θ_0, e.g. typically 10 to 20 arcsec in the *H* band. When applied to extragalactic astronomy, this makes the use of natural guide stars impossible for AO, at least in its 'classical' form, as the sky coverage would then be lower than 3 per cent owing to the lack of sufficiently bright guide stars, even at a Galactic latitude of 30°.

Several concepts have therefore been proposed in recent years to increase the sky coverage and the corrected FoV of AO systems. The laser guide star (LGS) method (Foy & Labeyrie 1985) creates an artificial star in the sodium layer of the atmosphere at an altitude of 90 km by means of a laser. However, this method suffers from the cone effect and the tilt determination problem (Tallon & Foy 1990; Rigaut & Gendron 1992), meaning that a natural guide star is always required close to the science target to measure the low orders of the turbulent wavefront (tip–tilts). Moreover, in the case of multi-object instruments such as those required for extragalactic astronomy, one LGS is required per scientific target as well as a dedicated wavefront sensor to measure the low orders. This can dramatically increase the cost of such a multi-object instrument. Multi-conjugate adaptive optics (MCAO) (Dicke 1975; Johnston & Welsh 1994; Fusco et al. 2001; Le Louarn 2002) have also been proposed to improve the FoV of AO systems, using several deformable mirrors (DMs) conjugated to the dominant turbulent layers, but the compensated FoV provided by such systems remains generally insufficient for extragalactic studies. As an example, the compensated FoV provided by the Gemini-South MCAO system or the Multi-conjugate Adaptive optics Demonstrator (MAD) system for the Very Large Telescope (VLT) will have a diameter of only 2 arcmin (Ellerbroek et al. 2003; Marchetti et al. 2003). Finally, the ground-layer adaptive optics method (GLAO) (Rigaut 2002) has also been proposed to widen the FoV of AO systems, but this approach assumes that most of the turbulence is located close to the telescope pupil. Moreover, the corrected FoV remains generally insufficient for extragalactic studies, and most of the GLAO systems studied up to now have always used at least one LGS to reach a decent performance (Le Louarn & Hubin 2004; Morris et al. 2004).

Such considerations therefore initiated the FALCON concept (Hammer et al. 2002). FALCON ('Fibre optics spectrograph with Adaptive optics on Large fields to Correct at Optical and Near-infrared') is a concept of a new-generation multi-object integral field unit (IFU) spectrograph, working with adaptive optics over a very wide field of view (10×10 arcmin^2) at the Nasmyth focus of the VLT and suitable for extragalactic studies. Instead of correcting the whole FoV, however, the AO correction is performed only on the regions of interest, e.g. the spectroscopic IFUs observing galaxies, thanks to a Deformable Mirror (DM) conjugated to the pupil for each IFU. However, with such an architecture, the sky coverage problem of classical AO remains. We have focused on this problem, which is solved by using a new type of wavefront reconstruction, inspired by MCAO techniques (Fusco et al. 2001; Tokovinin et al. 2001), where the wavefront sensor (WFS) measurements from several off-axis natural guide stars (NGS) around each galaxy are used to extrapolate the on-axis galaxy wavefront in the pupil. The preliminary performance of this concept has been given in Assémat et al. (2004) and Hammer et al. (2004).

In this paper, we will show more accurately the expected performance achieved by FALCON thanks to the combination of three-dimensional (3D) spectroscopy with AO. First, we will present the technical specifications of FALCON, derived from the higher level scientific requirements. We will then show the gain that AO can bring to IFS. Following that, we will accurately describe the principle of the FALCON AO system. The next section will show the expected performance of such a system in the case of median atmospheric conditions for the Cerro Paranal observatory. The discussion will then compare this performance with those from a GLAO system working in the same conditions, and will deal with additional source of errors the influence of which remains to be quantified.

2 HIGH-LEVEL SPECIFICATIONS

2.1 Wavelength range

As explained in the Introduction, dynamical information is required to improve our knowledge of the mechanisms responsible for the formation of galaxies. The velocity field of the galaxies has therefore to be probed by measuring the redshifts of emission lines, which we choose to peak in the 1.00–1.85 μm wavelength range (covering the *J* and *H* bands), thus avoiding the thermal domain ($\lambda > 1.95$ μm) where the instrumental thermal background will dominate the noise. Several emission lines can then be used, such as [O II] ($\lambda = 3727$ Å), Hβ ($\lambda = 4861$ Å), [O III] ($\lambda = 5007$ Å) and in particular Hα ($\lambda = 6563$ Å). Indeed, this latter suffers less from extinction than the other emission lines (Liang et al. 2004), and can be used to map the dynamical information up to $z = 1.8$. The use of shorter wavelength emission lines will allow the observation of galaxies up to $z = 2.5$, although extinction may then be a problem (Liang et al. 2004).

2.2 Angular resolution

Morphological studies of galaxies located in the *Hubble Deep Fields* and the Great Observatories Origins Deep Survey (GOODS) fields have shown that galaxies with $z \geqslant 1$ have half-light radii $r_{1/2}$ smaller than 0.5 arcsec (Marleau & Simard 1998; Ferguson et al. 2004), with an average $\langle r_{1/2} \rangle = 0.25$ arcsec at $z = 2$ (Bouwens et al. 2004). As we want to study the dynamical processes occurring within the

Downloaded from https://academic.oup.com/mnras/article/376/1/287/973575 by CNRS - ISTO user on 04 October 2022

galaxies, we must be able to resolve their half-light radius, up to $z = 2$. Therefore an angular resolution of at least 0.25 arcsec is required, implying a pixel sampling of 0.125 arcsec. Such a spatial resolution is far beyond the capabilities of current ground-based, seeing-limited, integral field spectrographs, as it is definitely better than the atmospheric seeing. This strongly suggests the use of AO, as we will see later in Section 3.

2.3 Spectral resolution

We have to observe in the near-infrared (NIR) to fulfil our scientific requirements. However, the spectral window we want to explore is crowded with thin, intense terrestrial OH emission lines (Maihara et al. 1993; Rousselot et al. 2000; Hanuschik 2003). Observations must therefore be performed between these lines, implying that we must be able to separate them.This leads therefore to a minimum spectral resolution $R = 5000$. Considering now the impact on the determination of the galaxy dynamics, this is equivalent to resolving velocity dispersions $\sigma \geqslant 25.5$ km s^{-1} at $z = 0$.

However, for such an instrument dedicated to the observation of distant galaxies, the optimal spectral resolution is a compromise between the scientific goals on the one hand, and the drastic loss in spectral signal-to-noise ratio (SNR) with increasing R on the other. As an example, spectral resolutions $R \leqslant 15\,000$ will allow us to resolve velocity dispersions $\sigma \geqslant 8/(1 + z)$ km s^{-1}, i.e. greater than 4 km s^{-1} for a galaxy located at $z = 1$. A value of 15 000 seems therefore to be a reasonable upper limit to consider for the spectral resolution R. Recent observations of $z = 0.6$ galaxies with GIRAFFE (Flores et al. 2006) have in fact shown that a slightly lower spectral resolution $R = 10\,000$ is definitely required to probe precisely the kinematics of distant galaxies with various morphologies, including compact galaxies. Moreover, a spectral resolution $R = 10\,000$ also allows us to resolve the [O II] 3727 doublet, and then to retrieve the kinematics of galaxies with higher redshift.

2.4 FoV and multiplex capability

Observations of Lyman break galaxies with $z \geqslant 2$ show a strong spatial clustering, with correlation lengths greater than 4 Mpc (Giavalisco 2002). Similar results are also confirmed by cosmic web simulation codes, based on Λ cold dark matter (ΛCDM) theory (Hatton et al. 2003). The observation of distant galaxies over scales greater than this correlation length should therefore be achievable, in order to avoid statistical biases due to the cosmic variance effects. As an example, such effects have been observed on the Wide Field Planetary Camera 2 *Hubble Deep Fields* (Labbé et al. 2003), where the FoV ($\approx$6 arcmin^2) is insufficient. It is then necessary to encompass the correlation lengths for all redshifts, leading to a instrument with a minimum FoV of 100 arcmin^2.

The FoV of the instrument is also linked to the number of IFUs as well as the desired multiplex gain. As an example, Steidel et al. (2004) found a density of 3.8 galaxies per arcmin^2, for objects with redshifts $1.5 < z < 2.0$ and magnitudes $R \leqslant 25.5$. If we assume now that we only observe objects with magnitudes $R \leqslant 23.5$ or even $R \leqslant 23.0$ (because of SNR issues), we find a lower source density, comprising between 0.31 and 0.84 galaxies per arcmin^2. From our past experience on European Southern Observatory (ESO) large programmes with GIRAFFE (Hammer et al. 1999), we think that 15 to 30 IFUs should be a reasonable number while providing an efficient gain in terms of exposure time. However, in order to optimize the exposure time, it is required to observe objects in the same magnitude range, and the appropriate density to consider becomes the number of objects per magnitude and per arcmin^2. Moreover, a non-negligible fraction of the objects will see their emission lines match with atmospheric OH lines, making them impossible to observe. As a consequence, this might make the source density definitely smaller than the values written above, and low enough to warrant a wide FoV, equal to 10×10 arcmin^2. The VLT Nasmyth focal plane is therefore ideally suited for a FoV, as the vignetting on a 10 arcmin diameter FoV is less than 1 per cent. Spreading several IFUs over the Nasmyth focus will therefore allow us to perform the simultaneous 3D spectroscopy of several galaxies with similar redshifts, thus providing a very important gain in exposure time.

2.5 Conclusion

In this section we have given high-level specifications for the FALCON instrument, derived from scientific requirements. As has been shown, a multi-object spectrograph with both high spatial (FWHM $\leqslant$ 0.25 arcsec) and spectral ($R \geqslant 5000$) resolutions is required, moreover over a wide FoV ($\geqslant$100 arcmin^2).

We would especially like to insist now on the spatial resolution that we require (0.25 arcsec), which is not achievable with current seeing-limited instruments such as GIRAFFE. This requires the image quality to be enhanced, and the best way to achieve this, in particular in terms of SNR, is to use AO. We therefore show in the following section the gain brought by AO to IFS.

3 3D SPECTROSCOPY AND AO

3.1 Introduction: why use AO with 3D spectroscopy?

AO is a technique that allows us to restore in real-time the flatness of a wavefront distorted by the effects of the atmospheric turbulence, thus improving the image quality at the focal plane of an instrument. For classical imaging applications, the main interest of AO is to allow us the partial restoration of spatial frequencies in the images up to the cut-off frequency of the telescope (D/λ, D being the telescope diameter), far beyond the turbulent cut-off frequency. This is the consequence of the morphology of the compensated point-spread function (PSF), which is quite complex: it cannot be summarized only by its FWHM, as it depends on the structure function of the phase residuals, and in particular on the compensation order. The more important this latter, the more intense is the 'coherent core' (with a width of λ/D) on top of the PSF halo. Deconvolution processes can then be applied, the performance of which increases together with the SNR, i.e. with the restoration quality. Expecting this high-frequency restoration makes it mandatory to obey the Nyquist criteria for the image sampling.

Expectations are different when studying faint galaxies with 3D spectroscopy at $R \approx 10\,000$. The intrinsic faintness of the dispersed signal prohibits, anyway, any attempt to sample it spatially at the Nyquist frequency. Hopefully for us, this latter is not an issue, since we are not interested in the ultimate telescope resolution, but only in a moderate resolution of 0.25 arcsec. Our concern is therefore to maximize the flux from the object within a square aperture of 0.25×0.25 arcsec^2 – our spatial resolution element. This has two consequences. First, it increases the signal from the object within the spatial resolution element, whereas the noise level (especially thermal and sky background) will remain constant: the spectroscopic SNR will increase. Secondly, the flux spread in the neighbouring pixels will be minimized, thus avoiding spatial contamination.

These improvements of the image quality expected in spectroscopy (resolution, SNR improvement, reduction of confusion) are difficult to relate to the parameters commonly used in AO to characterize the quality of the restored image. Classical parameters

Downloaded from https://academic.oup.com/mnras/article/376/1/287/973575 by CNRS - ISTO user on 04 October 2022

are, for example, the FWHM or the Strehl ratio (SR; this latter is defined as the central intensity of a restored PSF, divided by the central intensity of the diffraction-limited PSF, taking both PSFs with the same total energy). For 3D spectroscopy applications, the criterion traditionally used, and which defines the spectroscopic image quality, is in fact the fraction of the total PSF flux 'ensquared' within the spatial resolution element. We will therefore use this criterion, the *ensquared energy*, in the following sections of this paper.

3.2 The need for a high-order compensation

FALCON had initially begun with the wrong idea that a low-order or a moderate compensation should be sufficient to achieve a goal that, at least at first glance, appeared to be modest: obtain a resolution of 0.25 arcsec. We demonstrate in the following sections that getting such a resolution implies a finer spatial sampling (0.125 arcsec) compared with existing instruments, and consequently a huge loss in SNR per spatial sample. This loss has to be compensated by an increase of the ensquared energy. We point out that a high ensquared energy can be obtained only by using a high-order compensation. This effect is implicitly demonstrated at the end of our paper, in the last results section, where we will see that the ensquared energy still takes advantage of a high-order correction. However, we want to insist on this particular point from now on, because this explains why we have especially focused a large part of our study on the number of degrees of freedom that the system will have, and why we study all the compensation levels up to 120 Zernike modes in this paper.

We illustrate here how the ensquared energy is a parameter sensitive to the spatial frequency range of the phase residuals. We will compare two illustrative cases: they are comparable, in the sense that their wavefront flatness is the same (i.e. the same amount of residual phase variance). The two cases just differ by the spatial frequency of the phase residuals.

Any publication about AO compensation focuses on phase residual variance, which is considered as the key parameter that optimizes the image quality. We exhibit here two striking examples of PSFs where the ensquared energies are fundamentally different (more than a factor of 2), while their associated phase variance, Strehl ratio and FWHM are the same.

For our illustration, we have performed some Monte Carlo numerical simulations of an AO-corrected PSF, where the wavefront (from a fully developed Kolmogorov spectrum) is corrected by zeroing some coefficients of its expansion into Zernike polynomials (Noll 1976). As we just study the influence of the compensation order, here we focus only on the spatial aspect of the correction, ignoring errors due to time delay, anisoplanatism or noise. The conditions of the simulation are a 8-m telescope (VLT case) and a seeing of 0.81 arcsec at 0.5 μm (median seeing of the VLT site, Martin et al. 2000), leading to an r_0 equal to 52 cm at the imaging wavelength of 1.65 μm (H band). We have compared two clear-cut cases of correction, similar since they both lead to the same amount of residual phase variance $\sigma^2_{\rm res} = 0.0132(D/r_0)^{5/3}$ rad^2, but different because the compensation concerns different domains of spatial frequencies, as illustrated in Fig. 1.

(i) For case A, we mimic a typical low-order AO system, and we compensate for the polynomials Z_2 to Z_{36}. Phase residuals are high-order perturbations $Z_{>37}$.

(ii) For case B, we consider that the phase residuals are now low-order perturbations in the range Z_{17-36}. These last numbers are chosen so that the spatial frequency contents of the phase do not overlap with case A, but have exactly the same variance.

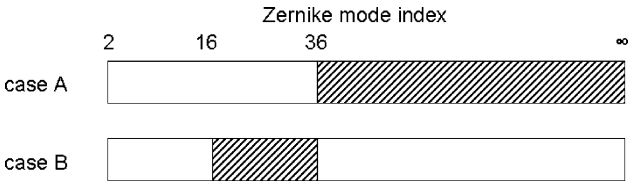

Figure 1. The hatched areas indicate the spatial frequency range of the residuals, described by the index of the Zernike mode. Case A has been chosen because it mimics a case typical of a low-order AO system. The numbers for case B (residuals is the range Z_{17-36}) are chosen to provide the same wavefront flatness (same phase variance) as in case A. The two PSFs will have the same phase variance, the same SR and the same FWHM.

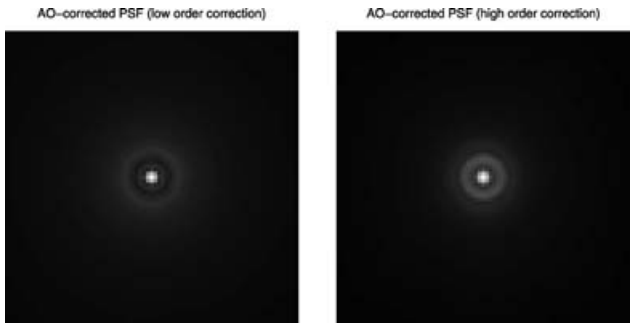

Figure 2. AO-corrected PSFs in the case of low-order correction (perfect correction of ZPs up to $j_{\rm max} = 36$, left) and high-order correction (perfect correction of ZPs 2 to 16 and 37 to ∞, right). The plots are for an 8-m-diameter telescope and a seeing of 0.81 arcsec at $\lambda = 0.5$ μm, H band ($\lambda = 1.65$ μm). The simulated FoV is equal to 1.70×1.70 arcsec^2.

The AO-corrected PSFs in the H band are shown in Fig. 2, whereas Fig. 3 shows the radial profiles (left) and ensquared energy profiles (right). These figures aim to demonstrate how different the shapes of the PSFs can be, although they simultaneously exhibit identical residual phase variances, identical central intensities (predictable from the phase variance: both Strehl ratios are close to 30 per cent) and identical FWHMs: the shapes of the coherent cores are identical; only the energy distribution of the halo is different, because it is strongly determined by the spatial contents of the phase residuals.

In terms of astrophysical implications, a PSF such as in case B (low-order residuals, right-hand panel of Fig. 2) would be catastrophic for exoplanet detection, where the intensity in the first rings has to be minimized because of contrast issues. In contrast, such a

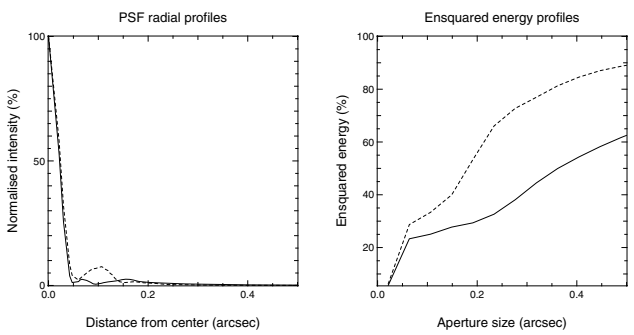

Figure 3. Radial profiles (left) and ensquared energy profiles (right) of the AO-corrected PSFs. The solid line corresponds to low-order correction, the dashed line to high-order correction.

Downloaded from https://academic.oup.com/mnras/article/376/1/287/973575 by CNRS - ISTO user on 04 October 2022

PSF is interesting for 3D spectroscopy as the ensquared energy is increased: this is particularly noticeable in the right-hand panel of Fig. 3.

One has therefore to keep in mind that for a fixed amount of phase variance removed, the ensquared energy will be strongly enhanced in the case of a high-order compensation, which is particularly effective at reducing the halo compared with low-order mode correction. The conclusion is that the common rule of thumb, according to which the phase variance error budget should be balanced between 'under-modelling' error and other sources, becomes obsolete when it is a matter of designing an AO system for spectroscopy. Despite the moderate resolution (≈0.25 arcsec) required, a rather large number of actuators is required to bring the light from the further parts of the halo into the inner parts, so as to increase the spectroscopic SNR, and only a high-order mode compensation can allow us to achieve this.

However, compensating for high-order modes is not without some difficulties from the AO point of view, the major limitation being anisoplanatism: high-order modes unfortunately decorrelate faster with the separation angle (Chassat 1989; Roddier et al. 1993). Unfortunately, the usual observing conditions of distant galaxies are at high Galactic latitudes, where natural guide stars become scarce and are unlikely to lie within the isoplanatic patch θ_0. This requires us to work most of the time with large separation angles, which precisely forbid the compensation of high-order modes. This drawback makes classical AO inappropriate for statistical studies of distant galaxies.

In Section 4 we will describe a new approach to AO, which solves anisoplanatism problems, allowing the use of natural guide stars at distances greater than θ_0, and which is still efficient to correct high-order modes.

Before this, we want to be able to establish requirements regarding the ensquared energy needed for a proper statistical study of high-redshift galaxies, in order to derive later some specifications for the AO system that we propose.

3.3 Case study: 3D spectroscopy of UGC 6778 observed at high redshift

Thanks to numerical simulations, we show in the following subsections some quantitative results about the gain in spectroscopic SNR that can be achieved when AO and 3D spectroscopy are used together. We would like to emphasize here that we do not attempt to perform a complete simulation of a 3D spectrograph fed by an AO system, because of the lack of 3D spectroscopic data currently available in the literature for high-redshift galaxies, and especially in the NIR wavelength range, where the Hα emission line is observed for redshifts $z \geqslant 0.5$. We therefore make very simple assumptions about the instrument as well as the observed objects, in order to compute first estimates of the SNR achieved thanks to AO correction. Such results can be used to derive very preliminary required ensquared energy values, which can then be translated into instrumental requirements for the AO system. A ΛCDM cosmology with $H_0 = 70$ km s^{-1} Mpc^{-1}, $\Omega_{\rm m} = 0.3$ and $\Omega_\Lambda = 0.7$ is assumed in the rest of this paper.

We have used for this study the Hα image of the UGC 6778 galaxy provided by members of the Gassendi Hα Survey of SPirals (GHASP; Garrido et al. 2002, 2003, 2004, 2005), with a spatial sampling $s_0 = 0.960$ arcsec pixel^{-1}. Table 1 lists the photometric and dynamical properties of this galaxy. These data were then used to simulate two science cases, where we assumed that the galaxy would be respectively located at $z = 0.9$ or 1.5, and that a microlens + fibres integral field spectrograph similar to GIRAFFE would be used to perform 3D spectroscopy on the galaxy.

The first steps required to perform these simulations are the following.

(i) Use of the original Hα image to simulate the distant galaxy image, taking into account the decrease of the apparent diameter due to redshift as well as the change of spatial sampling [see Giavalisco et al. (1996) for more information]. We assumed a spatial sampling in the simulated galaxy image equal to half of the telescope diffraction limit (Nyquist sampling), i.e. $\lambda/2D$.

(ii) Computation of the apparent magnitude m in the observing band (J or H) from the absolute magnitude of a nearby galaxy M, using the distance modulus, and taking into account the *morphological K-correction* $K(z)$ due to redshift in the distance modulus equation: $m - M = 5\log(D_L/10) + K(z)$, where D_L is the luminosity distance. We used values from Mannucci et al. (2001) for the K-correction. The flux in the continuum $f_{\rm cont}$ (in erg s^{-1} cm^{-2} Å^{-1}) can then be computed from the apparent magnitude m.

(iii) Computation of the total flux (in erg s^{-1} cm^{-2}) of the galaxy in the redshifted Hα line, and normalization of the simulated Hα image.

(iv) Simulation of the distant galaxy continuum image assuming a pure Freeman exponential profile, taking into account the disc scalelength $R_{\rm D}$ and the angular distance $D_{\rm A}$. The flux normalization is done using $f_{\rm cont}$.

Fig. 4 shows the original Hα image from the GHASP survey ($z \approx 0.0$, pixel size $s_0 = 0.96$ arcsec), as well as the simulated Hα and continuum map corresponding to the first science case ($z = 0.9$, pixel size $s_z = 0.016$ arcsec).

We are going now to focus on the two H II regions at the bottom left of the Hα image. Garrido et al. (2002) have indeed shown that they have very similar velocities (≈890 km s^{-1}). We therefore make the assumption (sufficient for the rest of this study) that the integral field spectrograph we use has a sufficient spectral resolution R so that the flux sampled around the wavelength $\lambda_0(1 + v/c)$ (where λ_0 is the

Table 1. Photometric and dynamic characteristics of UGC 6778. From left to right: the identifier of the galaxy, its morphological type, the recession velocity corrected for the infall of the Local Group toward Virgo, $V_{\rm VIR}$, the distance D in Mpc, the absolute magnitude in the B band, M_B, the exponential disc scalelength, $R_{\rm D}$, the disc surface brightness, $\mu_{\rm D}$, the inclination, i, the position angle, PA, and the maximum velocity observed on the edge of the disc.

UGC ID	Type[a]	$V^b_{\rm VIR}$ (km s^{-1})	D[b] (Mpc)	M^a_B (mag)	$R^c_{\rm D}$ (kpc)	$\mu^c_{\rm D}$ V arcsec^{-2}	i^a (°)	PA[a] (°)	$V^a_{\rm max}$ (km s^{-1})
3893	SBc	1193	17.04	−20.6	1.84	20.17	30	165	305

References: [a] from Garrido et al. (2002); [b] from LEDA (http://www-obs.univ-lyon1.fr/hypercat/); [c] from Baggett et al. (1998).

Downloaded from https://academic.oup.com/mnras/article/376/1/287/973575 by CNRS - ISTO user on 04 October 2022

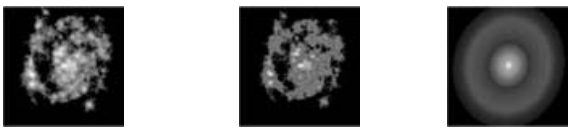

Original $H\alpha$ image
$z \approx 0.0$, $\lambda = 0.656\ \mu m$
$2.62 \times 2.62\ arcmin^2$
$s_0 = 0.96\ arcsec$

Simulated $H\alpha$ image
$z = 0.9$, $\lambda = 1.250\ \mu m$
$1.80 \times 1.80\ arcsec^2$
$s_z = 0.016\ arcsec$

Continuum map

Figure 4. Original Hα image (left), simulated Hα image (middle) and continuum map (right) of the UGC 6778 galaxy as if it were observed at $z = 0.9$ (in the *J* band), with the same physical size as today. The simulated field is 1.80×1.80 arcsec^2.

observing wavelength, i.e. 1.25 or 1.65 μm) is the flux emitted only in the Hα line by these two regions, v being their average velocity. We therefore isolated these two regions in the simulated images that we created.

However, the simulated Hα and continuum images suppose infinite spatial resolution, and do not take into account atmospheric seeing or AO partial correction effects.

We therefore convolved those images with different PSFs corresponding to all the possible orders of AO correction, from 0 to 120 Zernike polynomials (ZPs), at 1.25 and 1.65 μm. The principle of the simulation is the same as in Section 3.2, and we assumed the same conditions (8-m telescope, seeing of 0.81 arcsec at $\lambda = 0.5$ μm, no anisoplanatism, noise or temporal error). As a consequence of this AO compensation, a better contrast in the images as well as a better ensquared energy is observed, as already explained in Section 3.1. The result of the AO impact is illustrated, for a few cases, in Fig. 5.

Those images could then be used to compute the flux entering the microlens sampling each H II region, and then compute the final number of electrons on each pixel of the detector located at the output of the spectrograph, requiring therefore knowledge of the spectral profile of the line. We assumed a Gaussian line profile for the line, the consequence of some internal velocity dispersion σ_V in those H II regions, as well as the finite spectral resolution R of the spectrograph. As a result, the line profile on the spectrograph detector has a Gaussian shape, with a standard deviation $\sigma_{\rm tot} = \sqrt{\sigma_{V,\lambda}^2 + \sigma_S^2}$, $\sigma_{V,\lambda} = \lambda_0 \times \sigma_V / c$ being the standard dispersion in wavelength due to the internal velocity dispersion of the H II regions, and $\sigma_S = \lambda_0 / 2.354R$ being the standard deviation due to the spectral resolution, with λ_0 being the observing wavelength and c the speed of light. Therefore, if we call $F_{\rm ML}$ the total flux in the H II region sampled by the microlens of the spectrograph, the line profile $f(\lambda)$ as a function of wavelength will be written

$$f(\lambda) = \frac{F_{\rm ML}}{\sigma_{\rm tot}\sqrt{2\pi}} \exp\left[-\frac{(\lambda - \lambda_0)^2}{2\sigma_{\rm tot}^2}\right]. \quad (1)$$

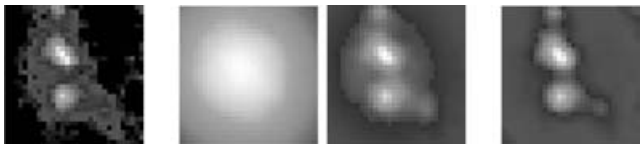

Figure 5. Illustration of the effect of AO compensation on the images. The simulated images cover a field of 0.50×0.50 arcsec^2 (4×4 microlenses of 0.125×0.125 arcsec^2). A analysis has been done that covers compensation orders from 0 to 120 Zernike modes. A few cases have been picked up and are presented here for illustration purposes. From left to right: diffraction-limited image, seeing-limited image, AO-corrected image for 46 and 100 ZPs.

This line profile is then going to spread over two directions on the spectrograph detector: the horizontal direction will correspond to the spectral information, and the perpendicular direction will correspond to the spatial information. This allows us to compute the number of electrons due to the Hα line per pixel on the spectrograph detector, and then the spectroscopic SNR. If $\Delta\lambda$ is the spectral sampling of the detector, $S_{\rm tot}$ the telescope area, $t_{\rm exp}$ the exposure time, and $T_{\rm tot}$ the total transmission of the system (which takes into account the detector efficiency), the number of electrons $N_{\rm H\alpha}$ coming from the redshifted Hα line on the pixel sampling the line at wavelength λ_0 is then equal to

$$N_{\rm H\alpha} = 2\int_0^{\Delta\lambda/2} f(\lambda)\,{\rm d}\lambda \times S_{\rm tot} \times t_{\rm exp} \times T_{\rm tot} \times \lambda_0/hc, \quad (2)$$

where h is the Planck constant.

We then have the flux from the line going on to the detector pixel. However, as we are interested in computing the spectroscopic SNR, we therefore need to take into account all the sources of noise, which can be divided into three categories: the line and continuum photon noise, the background photon noise, and the detector noise. As both line and continuum signals have Poissonian statistics, their associated photon noise therefore has a variance equal to their respective values, i.e. N_S and $N_{\rm cont}$, where the number of electrons $N_{\rm cont}$ due to the continuum is equal to

$$N_{\rm cont} = f_{\rm cont} \times S_{\rm tot} \times t_{\rm exp} \times \Delta\lambda \times T_{\rm tot} \times \lambda_0/hc, \quad (3)$$

$f_{\rm cont}$ being the flux from the continuum entering the microlens after convolution of the continuum image by the AO-corrected PSF. Concerning the background noise, this is the sum of the sky background as well as the instrumental thermal background. Then, if we call $N_{\rm B}$ the total number of electrons coming from the background, as it also has Poissonian statistics, its associated photon noise will then have a variance equal to $N_{\rm B}$. Finally, sources of detector noise, i.e. dark current noise and readout noise, have to be considered.

Knowing all these values, we can then compute the SNR per spatial resolution element and per spectral pixel, which is written

$$\mathrm{SNR} = \frac{N_{\rm H\alpha}}{\sqrt{N_{\rm H\alpha} + N_{\rm cont} + N_{\rm B} + N_{\rm pix,spat}\left(N_{\rm D} + N_{\rm exp}\sigma_{\rm R}^2\right)}} \quad (4)$$

where $N_{\rm B}$ is the number of electrons coming from the instrumental and sky background, $N_{\rm D} = {\rm DC} \times T_{\rm exp}$ is the number of electrons due to the dark current DC (in e$^-$ s^{-1} pixel^{-1}), $N_{\rm exp}$ is the number of elementary exposures, $\sigma_{\rm R}$ is the readout noise (in e$^-$ pixel^{-1}), and $N_{\rm pix,spat}$ is the number of pixels on which the flux is spread in the spatial direction on the detector.

Equation (4) therefore gives the SNR for the measured quantities. However, Fig. 5 shows that as the AO correction improves, the image contrast becomes better, with an increase of the effective light coming from the H II region. As a result, the flux going into the microlens sampling each H II region is therefore the sum of two terms: the effective flux emitted by the H II region, and a *pollution* term coming from adjacent regions, which is going to degrade the spectrum of the area sampled by the microlens, provided as an output of the 3D spectrograph. This has led us to define another signal-to-noise ratio, which we will call the *effective signal-to-noise ratio* (ESNR), and which gives a measure of the effective gain provided by the coupling of AO with 3D spectroscopy. Its expression is

$$\mathrm{ESNR} = \frac{N_{\rm H\alpha,eff}}{\sqrt{N_{\rm H\alpha} + N_{\rm cont} + N_{\rm B} + N_{\rm pix,spat}\left(N_{\rm D} + N_{\rm exp}\sigma_{\rm R}^2\right)}}, \quad (5)$$

Downloaded from https://academic.oup.com/mnras/article/376/1/287/973575 by CNRS - ISTO user on 04 October 2022

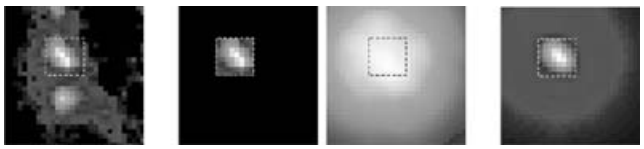

Figure 6. Explanation of the 'effective flux' notion. The first image on the left shows the original image, with the two H II regions and the superposed microlens (dashed lines). The second image shows only the area sampled by the microlens. The third and fourth images show this latter convolved by the uncorrected PSF (third image) and by an AO-corrected PSF (fourth image, correction of 60 ZPs). The effective flux from the Hα line is then equal to the flux of the region after convolution by the PSF going into the microlens.

where $N_{\mathrm{H}\alpha,\mathrm{eff}}$ is the number of electrons due to the effective Hα flux emitted by the area sampled by the microlens after convolution by the AO-corrected PSF, with no contribution from the adjacent areas around the microlens.This notion of *effective flux* is explained in Fig. 6.

It can be seen that the denominators in equations (4) and (5) are the same, and therefore that the ESNR is a lower bound of the SNR. This is explained by the fact that in the case of the ESNR, all the noise sources must appear in the denominator. Concerning the line, this latter has an associated noise, which is the sum of two terms: the photon noise of the effective flux, and a *pollution* term due to all the light coming from the area around the microlens and entering the microlens because of the convolution. As both quantities have Poissonian statistics, and as the convolution operator is distributive, the sum of these two terms is equal to the photon noise of the measured light entering the microlens.

We would, however, like to emphasize here that the ESNR defined in equation (5) and the classical SNR definition shown in equation (4) cannot be directly compared, in particular when the ensquared energy changes. As is shown in Fig. 6, the ESNR numerator is the flux coming only from the region sampled by the microlens after convolution by the AO-corrected PSF, whereas the SNR numerator is the flux coming not only from the microlens, but also from adjacent areas and polluting the microlens because of the convolution. As different images are convolved for ESNR and SNR computations, there is no direct relation (i.e. multiplication) between these numbers. Moreover, as explained in Section 3.1, an increase of the ensquared energy is due to a better compensation order provided by the AO system. Thus different ensquared energy values correspond to different AO-corrected PSFs, and the results of the convolution of the same high-resolution galaxy image by these different PSFs also cannot directly be comparable.

Once these two different quantities (SNR and ESNR) were defined, we performed some numerical simulations in order to quantify the gain in ESNR provided by the combination of AO with 3D spectroscopy. The results of these simulations are shown in the next section.

3.4 Results

Thanks to simulations, we are now able to show some preliminary results on the improvement in ESNR as a result of AO. Two science cases, corresponding to the observation of UGC 6778 at two different redshifts, are considered in the two next subsections.

For the first one, we assumed that the observed galaxy would be located at $z = 0.9$. In that case, the Hα emission line is redshifted to a wavelength of 1.25 μm, corresponding to the central wavelength of the *J* band. Moreover, we assumed that the galaxy had the same properties as the distant large spirals observed in the Canada – France Redshift Survey (CFRS; Lilly et al. 1998; Zheng et al. 2004). In particular, the physical size of the simulated galaxy is the same as that observed in the local Universe. As there are no direct measurements of Hα fluxes available in the literature for CFRS galaxies at these redshifts, we therefore computed the Hα luminosity from [O II] 3727 fluxes (Hammer et al. 1997), in order to normalize the simulated Hα image.

For the second case, we assumed that the observed galaxy would be located at $z = 1.5$. In that case, the Hα emission line is redshifted to a wavelength of 1.65 μm,corresponding to the central wavelength of the *H* band. Moreover, we assumed that the galaxy had Hα fluxes similar to those observed for the population of 'BM galaxies' introduced by Steidel et al. (2004). The apparent size of the galaxy was then chosen to cover a field of 1 arcsec^2, consistent with apparent sizes observed for distant galaxies at these redshifts in deep surveys (Bouwens et al. 2004).

We focus now on the two H II regions that we used to compute the SNR and ESNR. Together they contribute 10 per cent of the total Hα flux in the simulated Hα image. We have also assumed that they have an internal velocity dispersion with $\mathrm{FWHM}_V = 30\,\mathrm{km\,s^{-1}}$ (e.g. $\sigma_V \approx 13\,\mathrm{km\,s^{-1}}$), leading as explained previously to a dispersion in wavelength on the spectrograph detector equal to $\sigma_{\lambda,V} = \lambda_0 \times \sigma_V/c$, λ_0 being equal to 1.25 or 1.65 μm. The spectral resolution was then fixed to $R = 10\,000$, allowing us to resolve the velocity dispersions of the H II regions. This then allowed us to define two cases of spectral sampling, corresponding to the horizontal direction on the spectrograph detector: $\Delta\lambda = 0.3$ Å pixel^{-1} (for the *J* band) or $\Delta\lambda = 0.6$ Å pixel^{-1} (for the *H* band). Such spectral samplings allow us to sample the spectral resolution with more than two pixels, thus providing a better sampling than Nyquist sampling, and then make a precise estimation of the barycentre of the Hα emission line in order to recover the galactic velocity field. For the vertical direction on the spectrograph detector, corresponding to the spatial information, we considered a number of pixels $N_{\mathrm{pix,spat}} = 3$, similar to the number of pixels used on the GIRAFFE spectrograph detector. Such a number of pixels, here again better than Nyquist sampling, is quite convenient to resolve spectrum deblending problems on the spectrograph detector.

For the sky background, we assumed that the spectrograph is observing between atmospheric OH lines, so the sky noise is equal to the sky continuum. Cuby (2000) has measured the sky continuum at the Cerro Paranal observatory, and found respective values of 1200 photon s^{-1} m^{-2} μm^{-1} arcsec^{-2} at a wavelength of 1.25 μm, and 2300 photon s^{-1} m^{-2} μm^{-1} arcsec^{-2} at a wavelength of 1.65 μm. We used the characteristics of the ISAAC spectrograph at the VLT to simulate the instrument: the instrumental background was simulated by a blackbody of temperature $T = 273$ K and an emissivity equal to 25 per cent, a total transmission (atmosphere + telescope + instrument + detector) of 13 per cent at 1.25 μm (central wavelength of the *J* band) and 19 per cent at 1.65 μm (central wavelength of the *H* band) was assumed, and the detector had a dark current $\mathrm{DC} = 30\,\mathrm{e^-\,h^{-1}\,pixel^{-1}}$ and a readout noise $\mathrm{RON} = 10\,\mathrm{e^-\,pixel^{-1}}$.

3.4.1 First science case: 3D spectroscopy of UGC 6778 at $z = 0.9$

Here we give the results of simulations of the 3D spectroscopy of UGC 6778 as if it were observed at $z = 0.9$. We assumed that the galaxy had the same physical size as it has now. However, the flux in the Hα line is consistent with that observed for distant galaxies. Such physical conditions correspond to those observed in large spirals in the distant Universe (Lilly et al. 1998; Zheng et al. 2004).

Downloaded from https://academic.oup.com/mnras/article/376/1/287/973575 by CNRS - ISTO user on 04 October 2022

The original Hα image covers a field of 2.62×2.62 arcmin^2, and the galaxy has a distance $D = 17.04$ Mpc, which leads to a physical field of $d_1 \times d_1$ kpc^2, with $d_1 = 13.40$ kpc. Now, if we assume that the same galaxy has a redshift z, we can then compute its luminosity distance D_L and its angular distance D_A, and we find that the observed field therefore has an apparent size equal to $\theta_z \times \theta_z$ arcsec^2, with $\theta_z = d_1/D_\mathrm{A} = 1.80$ arcsec. Moreover, the spatial sampling is not the same as we simulate the galaxy as if it were observed by the VLT (8-m-diameter telescope) at its diffraction limit, meaning the pixel sampling s_z is equal to Nyquist sampling ($\lambda/2D$), leading to a pixel size $s_z = 0.016$ arcsec. Therefore the numbers of pixels in the original and simulated images are not the same: as shown in Fig. 4, the original image has 164×164 pixels, whereas the simulated image has 111×111 pixels.

This simulated image must be then normalized so that its flux is equal to the flux in the Hα line. As explained before, there are no direct measurements of Hα fluxes in the CFRS galaxies, therefore we used [O II] 3727 luminosities to compute Hα fluxes. Hammer et al. (1997) found that the average rest-frame equivalent width of the [O II] 3727 line in CFRS galaxies located at $z = 0.9$ was equal to EW([O II] 3727) = 40 Å . Moreover, Kennicutt (1992) found that there is a relation between the equivalent widths in the [O II] 3727 and Hα lines, in the form EW(Hα) = $2.5 \times$ EW([O II] 3727). We therefore assumed that the Hα line had a rest-frame equivalent width EW(Hα) = 100 Å .

Once EW(Hα) is known, the flux in the continuum f_cont must be computed to know the flux $f_{\mathrm{H}\alpha}$ in the Hα line, as both are linked by the relation $f_{\mathrm{H}\alpha} = f_\mathrm{cont} \times \mathrm{EW\,(H\,}\alpha) \times (1 + z)$. f_cont is directly linked to the apparent magnitude of the galaxy. We see in Table 1 that UGC 6778 has an absolute magnitude in the B band $M_B = -20.6$. However, as the Hα line is redshifted in the J band, we are interested in the absolute magnitude of the galaxy in the J band. For an SBc galaxy like UGC 6778, Mannucci et al. (2001) give the following colours: $(B - V) = 0.70$, $(V - K) = 3.03$, $(J - H) = 0.66$ and $(H - K) = 0.25$. We then find an absolute rest-frame magnitude $M_J = -23.42$. Mannucci et al. (2001) also give the following K-correction for an Sc galaxy: $K(z = 0.9) = 0.155$. The redshift z can then be used to compute the luminosity distance D_L and the distance modulus. We therefore find an apparent magnitude $J = 20.41$, corresponding to a flux in the continuum $f_\mathrm{cont} = 8.09 \times 10^{-19}$ erg cm^{-2} s^{-1} Å^{-1}, leading to an Hα flux of 4.17×10^{-17} erg s^{-1} cm^{-2}. This flux was then used to normalize the simulated Hα image.

As explained before, the continuum emission has also to be taken into account. This latter is not equally spread over the galaxy, as the intensity of the disc in spiral galaxies follows a decreasing exponential law (Freeman 1970), in the form $I(r) \propto \mathrm{e}^{-r/R_\mathrm{d}}$, R_d being the disc scalelength, the value of which for UGC 6778 is given in Table 1. It is therefore possible to compute $R_{\mathrm{d},z}$, the angular size of of the disc scalelength when the galaxy is observed at a redshift z, by the relation $R_{\mathrm{d},z} = R_\mathrm{d}/d_\mathrm{A}$, D_A being the angular diameter distance, and we found a value of $R_{D,z} = 0.25$ arcsec. This value, as well as the position angle (PA) of the galaxy and the inclination i (which are given in Table 1), was used to compute the continuum map of the galaxy. This latter was then normalized so that its total flux was equal to f_cont. The simulated Hα image and the continuum map are shown in Fig. 4.

Once those two images have been created, it is possible to compute the measured spectroscopic and effective SNR per spectral pixel. However, as our goal is to show the gain given by the combination of AO with 3D spectroscopy, we convolved these latter images by simulated AO-corrected PSFs, with the degree of correction going from 0 ZPs (seeing-limited PSF) to 120 ZPs, leading to an increase of the ensquared energy as the number of corrected modes increases. We also considered exposure times between 1 and 8 h, with individual exposure times of 1 h. Fig. 7 shows the evolution of these SNRs as a function of the ensquared energy in a 0.25×0.25 arcsec^2 square aperture. More precisely, if we look at the evolution of the ESNR which eventually gives the real improvement provided by AO correction, we see that a minimum ensquared energy of 26 per cent allows us to reach an ESNR of 3 after an exposure

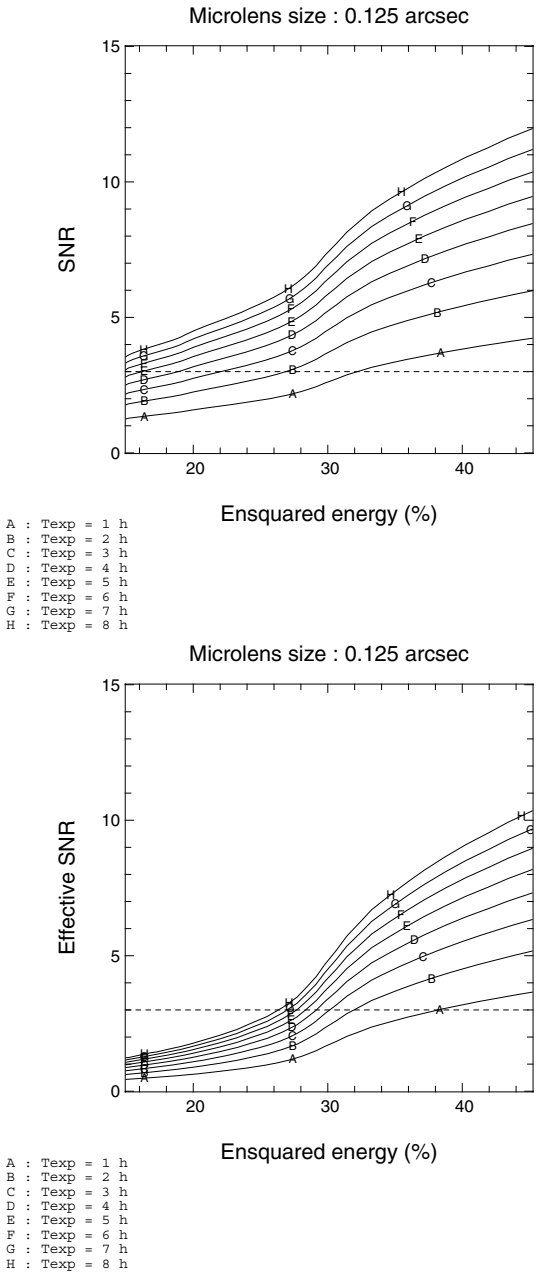

Figure 7. Measured spectroscopic SNR (top) and effective spectroscopic SNR (ESNR, bottom) on the Hα line for a microlens of 0.125 arcsec as a function of the ensquared energy in a 0.25×0.25 arcsec^2 square aperture. The galaxy under consideration is located at $z = 0.9$ (observation in the J band) and has the same characteristics as distant large spirals. Each curve corresponds to the average of the SNR of each microlens sampling the H II regions, with exposure times going from 1 to 8 h. The dashed line corresponds to SNR = 3.

Downloaded from https://academic.oup.com/mnras/article/376/1/287/973575 by CNRS - ISTO user on 04 October 2022

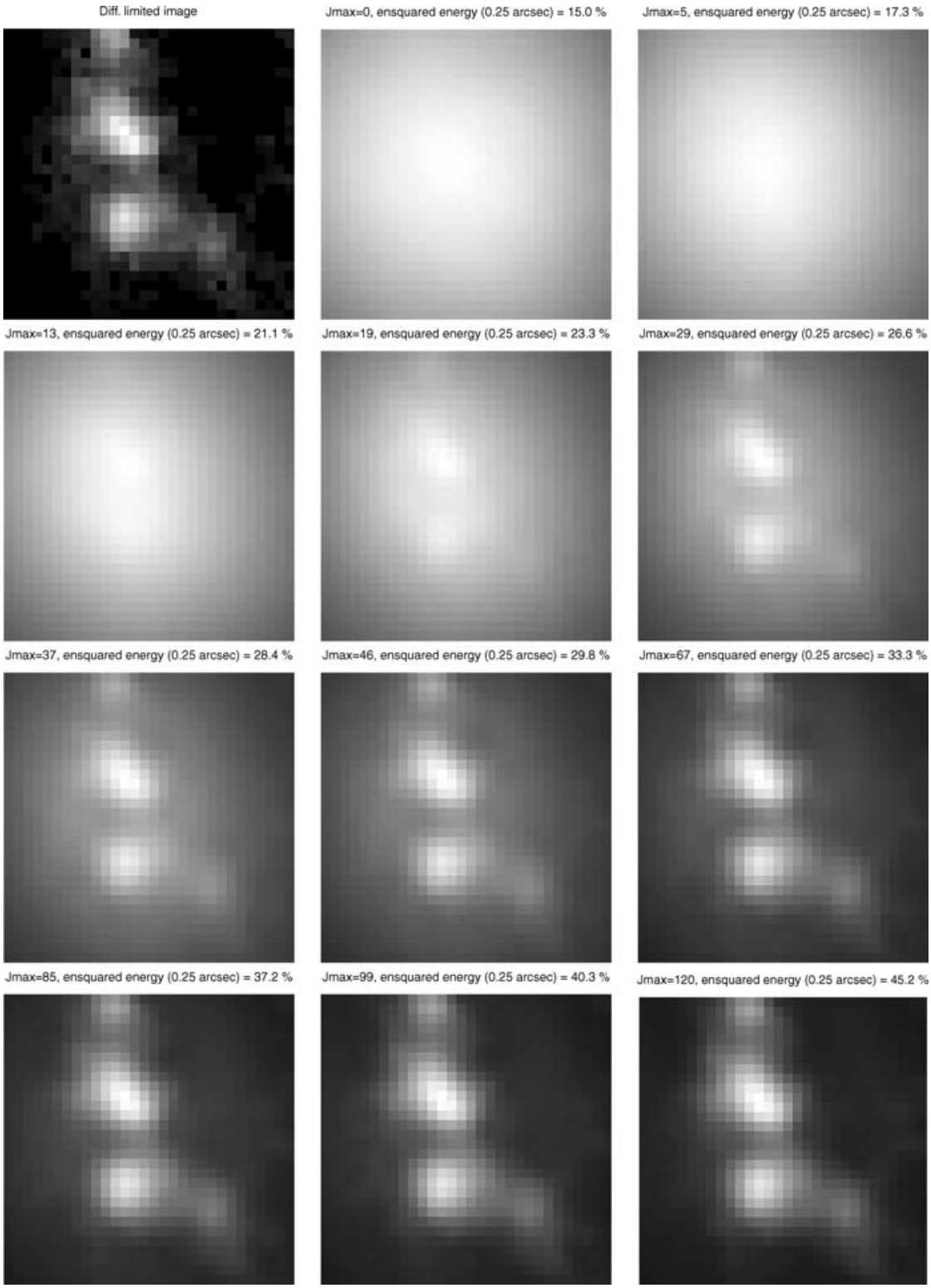

Figure 8. Images of the H II regions convolved with the AO-corrected PSF, for different levels of AO correction in the *J* band. The title of each image shows the number of corrected modes and the corresponding ensquared energy in 0.25×0.25 arcsec^2. The FoV is equal to 0.50×0.50 arcsec^2 (4×4 0.125-arcsec microlenses).

time of 8 h. However, a slight increase to an ensquared energy of 30 per cent allows us to reach the same ESNR value, but only after 3 h of exposure time.

As was shown previously, the AO correction not only increases the ensquared energy in the spatial resolution element, but also increases the sharpness of the AO-corrected PSF, therefore providing a better image contrast. This is indeed shown in Fig. 8, where it can be seen that the two H II regions start to be well separated after the perfect correction of the first 46 ZPs. This level of AO correction corresponds to an ensquared

© 2007 The Authors. Journal compilation © 2007 RAS, MNRAS **376,** 287–312

Downloaded from https://academic.oup.com/mnras/article/376/1/287/973575 by CNRS - ISTO user on 04 October 2022

energy equal to 28 per cent in a 0.25×0.25 arcsec^2 square aperture.

This study has therefore shown that the combination of 3D spectroscopy with AO is definitely effective in terms of angular resolution and SNR improvement. This means that the 3D spectroscopy of $z \approx 1$ galaxies with an angular resolution of 0.25 arcsec (definitely better than atmospheric seeing) should be achievable on a 8-m telescope located on the ground such as the ESO VLT. This requires the AO correction to provide a minimum ensquared energy of 28 per cent in a 0.25×0.25 arcsec^2 square aperture. In that case, a spectral resolution $R = 10\,000$, allowing us to resolve velocity dispersions with $\mathrm{FWHM}_V \geqslant 30$ km s^{-1}, can be used, as an effective spectroscopic SNR of 3 can be reached after an exposure time of only 3 h.

3.4.2 Second science case: 3D spectroscopy of UGC 6778 at $z = 1.5$

We give here the results of simulations of the 3D spectroscopy of UGC 6778 as if it were observed at $z = 1.5$. We assumed here that the galaxy covers an apparent surface area of 1 arcsec^2, which is consistent with apparent sizes measured in deep surveys. This apparent surface area was then used to simulate the apparent Hα and continuum images. We are now going to focus on the continuum and Hα flux normalization.

We used the data from Erb et al. (2003) and Steidel et al. (2004), who observed with the LRIS spectrograph on the Keck telescope a sample of BM/BX galaxies located between $z = 1.4$ and 2.5. Erb et al. (2003) found on their sample ($\langle z \rangle = 2.28$) an average apparent magnitude $\langle R \rangle = 24.37$, and an average apparent Hα flux $f(\mathrm{H}\,\alpha) = 4.6 \times 10^{-17}$ erg s^{-1} cm^{-2}. It will be seen that the apparent Hα flux is comparable to the one computed in the previous science case ($z = 0.9$) where we simulated the observation of a distant large spiral galaxy belonging to the CFRS. In fact the two science cases have been chosen using previous well-known studies of distant galaxies. At $z = 0.9$, the CFRS has studied average L^* galaxies, while at $z = 1.5$, Erb et al. (2003) have focused on a sample of specifically Hα-luminous galaxies.

Moreover, Steidel et al. (2004) found that galaxies with a redshift $\langle z \rangle = 2.23 \pm 0.31$ had an average colour $\langle R - K \rangle = 3.25 \pm 0.53$. We therefore found that those galaxies had an apparent magnitude $\langle K \rangle = 21.12$. It is therefore possible to compute their K absolute magnitude M_K using again the distance modulus, assuming a K-correction $K(z) = -0.57$ at $z = 2.3$ [extrapolation to $z = 2.3$ of the K-correction in the K band given by Mannucci et al. (2001) for an Sc galaxy], leading to $M_K = -24.38$. Moreover, as Sc galaxies have a colour $(H - K) = 0.25$ (Mannucci et al. 2001), we found that such a galaxy has a rest-frame H absolute magnitude equal to $M_H = -24.13$. Assuming a K-correction $K(z) = 0.078$ at $z = 1.5$ for an Sc galaxy observed in the H band (Mannucci et al. 2001), we therefore found an apparent magnitude $H = 20.99$ for the case where such galaxies would be located at $z = 1.5$, corresponding to a flux in the continuum $f_{\mathrm{cont}} = 1.67 \times 10^{-19}$ erg s^{-1} cm^{-2} Å^{-1}.

These flux values were used to normalize the simulated images of the distant galaxy. Then we did the same computations as previously explained, in order to compute the measured spectroscopic and effective SNR per spectral pixel on the spectrograph detector, and especially to show the improvements provided by AO correction. This time we considered exposure times from 3 to 24 h. Fig. 9 shows the result of the convolution of the galaxy image by the A_0-corrected PSF for the different orders of correction, and Fig. 10 shows the evolution of the ENSR as a function of the ensquared energy and the exposure time. We can see in the latter that an ESNR of 3 can be reached after a minimum exposure time of 9 h, requiring an ensquared energy after AO correction equal to 60 per cent in a 0.25×0.25 arcsec^2 square aperture. The same ESNR value can be reached with an ensquared energy after AO correction equal to 40 per cent, requiring then an exposure time of 18 h, or also with an ensquared energy after AO correction equal to 33 per cent, requiring then an exposure time of 24 h. However, in the previous section we saw that a minimum ensquared energy must also be reached so that the two H II regions can be separated. As shown in Fig. 9, we can see that the two H II regions start to be separated for an ensquared energy after AO correction better than 30 per cent.

This study has therefore shown that the combination of 3D spectroscopy with AO should allow us also to perform 3D spectroscopy of galaxies located at $z = 1.5$, also with an angular resolution of 0.25 arcsec (definitely better than atmospheric seeing) and with a spectral resolution $R = 10\,000$, allowing us to resolve velocity dispersions $\mathrm{FWHM}_V \geqslant 30$ km s^{-1}, as well as reaching an effective spectroscopic SNR of 3. This can be achieved with a minimum ensquared energy after AO correction of 35 per cent and an exposure time of 24 h, knowing that the same ESNR value can be reached with an ensquared energy of 40 per cent and a shorter exposure time (18 h).

3.5 Conclusion

We have studied in this section the improvement provided by the combination of 3D spectroscopy with AO. First we have shown that, thanks to AO, it is possible to reach an angular resolution better than seeing, but also to increase the spectroscopic SNR, allowing us to perform 3D spectroscopy of distant galaxies, thus studying their kinematics. We have then performed some simulations allowing us to give some preliminary results on the performance of an integral field spectrograph providing an angular resolution of 0.25 arcsec and a spectral resolution $R = 10\,000$, and which would observe distant galaxies located at $z = 0.9$ and 1.5. In that case, the Hα emission line is redshifted into the central wavelengths of the J and H bands (respectively 1.25 and 1.65 μm). To quantify the performance of such an instrument, we have defined a new criterion called the 'effective signal-to-noise ratio' (ESNR). We have also assumed for these simulations galaxies with properties consistent with those observed in distant surveys. We have therefore shown that an ESNR of 3 can be reached for a galaxy located at $z = 0.9$, requiring a minimum ensquared energy in 0.25×0.25 arcsec^2 after AO correction equal to 30 per cent and an exposure time of 3 h. The same ESNR value can be reached for a galaxy located at $z = 1.5$, requiring then a minimum ensquared energy after AO correction of 35 per cent and an exposure time of 24 h; however, a slight increase of the ensquared energy to 40 per cent should allow us to reach the same ESNR value after an exposure time equal to 18 h.

A study of the AO-corrected PSF has shown that high-order modes need to be corrected to improve the ensquared energy. This has been confirmed by our simulations of the 3D spectroscopy of distant galaxies, where we found that at least 46 ZPs need to be corrected to reach an ensquared energy of 30 per cent in the J band and 40 per cent in the H band (such results are not definitive, as we used the dynamical properties of one galaxy observed in the local Universe as well as those of a few distant galaxies, but they can be used as a first basis, the data required to perform such studies being still rare in the community). Such a number of modes corresponds in fact to the minimum order of modes to correct, as we

Downloaded from https://academic.oup.com/mnras/article/376/1/287/973575 by CNRS - ISTO user on 04 October 2022

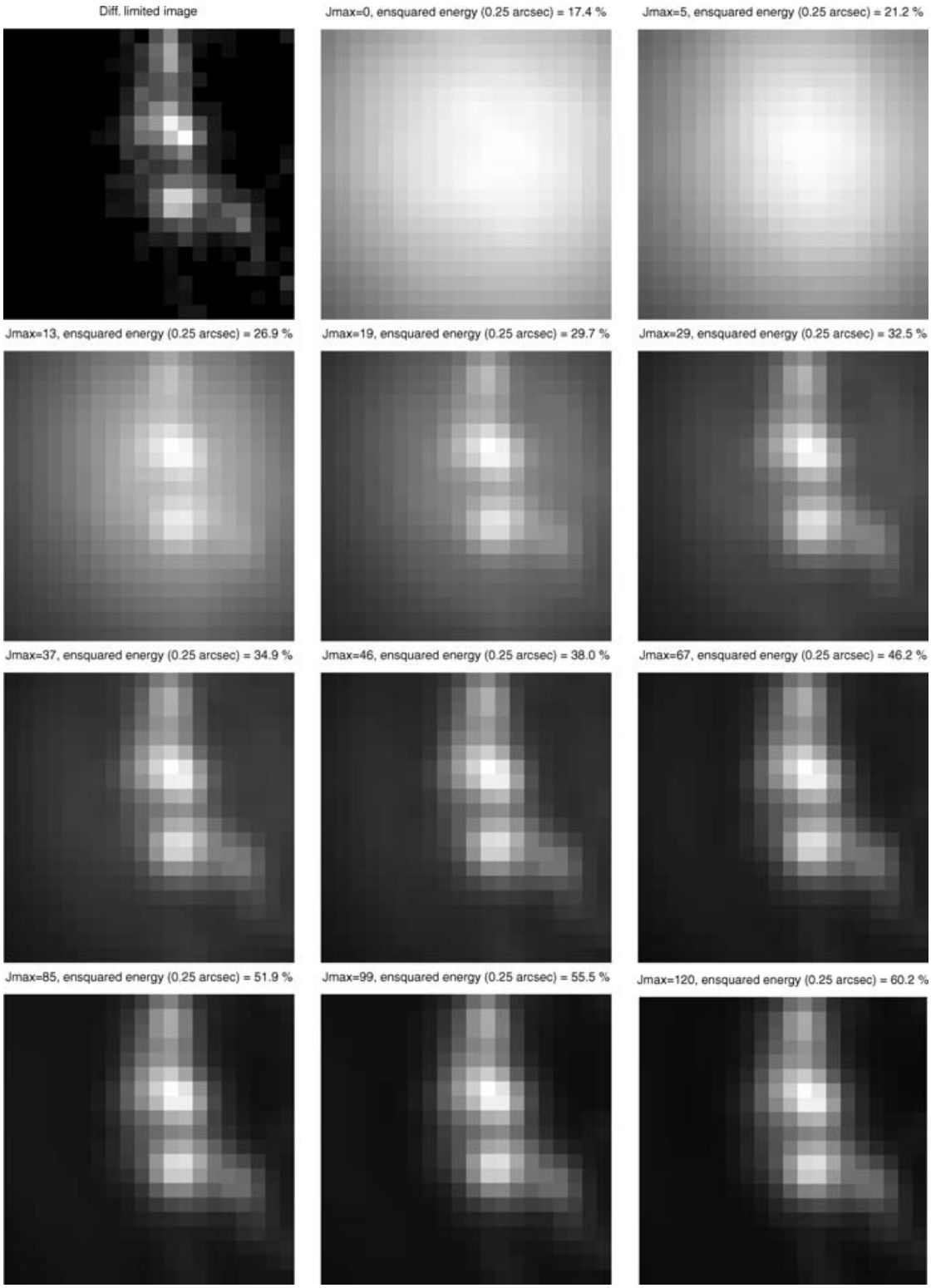

Figure 9. Images of the H II regions convolved with the AO-corrected PSF, for different levels of AO correction in the *H* band. The title of each image shows the number of corrected modes and the corresponding ensquared energy into a 0.25×0.25 arcsec^2 square aperture. The FoV is equal to 0.50×0.50 arcsec^2 (4×4 0.125-arcsec microlenses).

assumed a perfect AO system in our study. In a real AO system, other sources of error like time delay, measurement noise and anisoplanatism are going to degrade the performance of AO, meaning that a larger number of modes will be required to reach the same ensquared energy values and image quality. We must especially insist on the fact that anisoplanatism is going to become the most important limitation in the case of a real instrument using both AO and 3D spectroscopy. Indeed, as extragalactic studies need to work at high Galactic latitudes, the probability of finding a suitable star to perform wavefront sensing is equal to a few per cent, meaning that AO, at

© 2007 The Authors. Journal compilation © 2007 RAS, MNRAS **376,** 287–312

Downloaded from https://academic.oup.com/mnras/article/376/1/287/973575 by CNRS - ISTO user on 04 October 2022

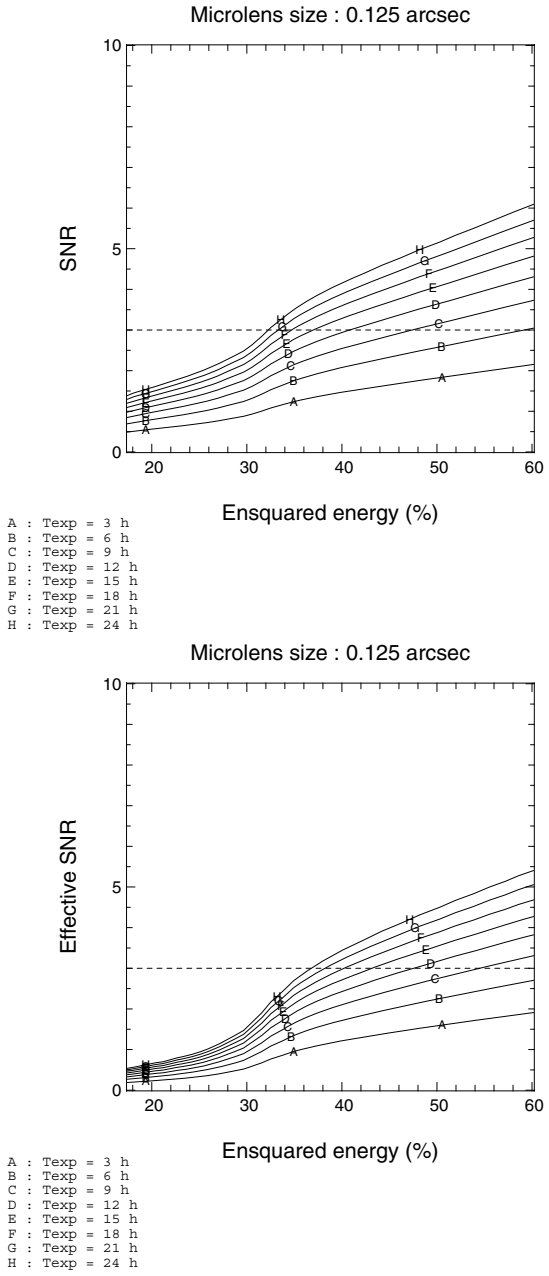

Figure 10. Measured spectroscopic SNR (top) and effective spectroscopic SNR (ESNR, bottom) on the Hα line for a microlens of 0.125 arcsec as a function of the ensquared energy in a 0.25×0.25 arcsec^2 square aperture. The galaxy under consideration is located at $z = 1.5$ (observation in the H band) and covers an apparent field of 1 arcsec^2. Each curve corresponds to the average of the SNR of each microlens sampling the H II regions, with exposure times going from 3 to 24 h. The dashed line corresponds to SNR = 3.

least in its *classical* form, cannot be used because of its very low sky coverage.

We are therefore going to describe in the next sections the principle and the performance of FALCON, a project involving a multi-object 3D spectrograph with AO, which solves the sky coverage problem imposed by classical AO. FALCON uses the principle of multi-object adaptive optics (MOAO). Such a technique allows us to widen the useful FoV of AO systems, thus to perform simultaneous 3D spectroscopy of several distant galaxies in a very wide FoV, providing therefore a huge gain in terms of observing time efficiency.

4 THE FALCON AO SYSTEM: PRINCIPLE

4.1 Increase of the AO-corrected FoV: MCAO and tomography

As stated in the Introduction, AO, in its classical form where one guide star and one deformable mirror (DM) conjugated to the pupil are respectively used to measure and correct the turbulent wavefront, suffers from a very low sky coverage (less than 5 per cent), even at Galactic latitudes of 30°. The reason for this limitation is that the probability of finding a suitable guide star in the isoplanatic patch is generally very low, because of the distribution of stars in our Galaxy.

Such a limitation has led to the development of multi-conjugate adaptive optics (MCAO). In MCAO, several deformable mirrors conjugated to the turbulent layers are used to correct the phase in the turbulent volume. Indeed, this is the distribution of the turbulence at the altitude that is responsible for anisoplanatism, as the wavefronts coming from different directions do not cross the same volume of atmosphere (especially for high turbulent layers), and therefore do not suffer from the same degradations. By correcting the phase in the turbulent volume, and especially in the strongest layers, it is possible to correct the wavefront for any direction, and to have a uniform compensation in a FoV larger than the isoplanatic patch.

Before correcting the phase with the different DMs, it is necessary to know the perturbation in each layer to apply adequate commands to each DM. This can be achieved thanks to *tomography* (Ragazzoni et al. 1999, 2000; Tokovinin & Viard 2001), where the light coming from several off-axis guide stars far outside the isoplanatic patch is used to probe the 3D phase perturbations in the atmosphere, generally by solving an inverse problem as in medical imaging. However, thanks to tomography, it is also possible to know the integrated phase perturbation in the pupil for any direction in the FoV. This means that the field where guide stars can be found is widened, and this allows a higher sky coverage for AO (Tokovinin et al. 2001).

However, the potential extension of the FoV with MCAO encounters some technical limitations, in particular on the optical system. As an example, the ESO MAD system for the VLT (Marchetti et al. 2003) or the Gemini-South MCAO system (Ellerbroek et al. 2003) will deliver a corrected FoV with a diameter of 2 arcmin, definitely smaller than the 10×10 arcmin^2 FoV required for extragalactic studies. We are therefore going to show in the next section a new approach for AO, where the goal is to provide a uniform correction not in a very wide FoV, but only for specific areas in it, i.e. the galaxies on which we want to perform 3D spectroscopy. This new approach is called multi-object adaptive optics (MOAO).

4.2 MOAO

First proposed by Hammer et al. in 2002, MOAO is a new method of AO correction which has essentially been since this date the object of a few conference proceedings papers (Assémat et al. 2004; Dekany et al. 2004; Hammer et al. 2004). We summarize its principles in this section.

Let us recall here that our goal is to measure the internal kinematics of distant galaxies spread over the VLT Nasmyth field. In other words, this means that a high angular resolution is required *only for the scientific targets*. As a result, we propose in this section a totally new approach for AO: instead of correcting the whole 10×10 arcmin^2 field (which anyway is impossible to do), we propose to

Downloaded from https://academic.oup.com/mnras/article/376/1/287/973575 by CNRS - ISTO user on 04 October 2022

correct locally only the regions of interest, i.e. the IFUs positioned on the scientific targets, and we have therefore *one AO system per IFU*. As a result, if we suppose that we want to perform the simultaneous 3D spectroscopy of 20 galaxies, we arrive at the concept of an instrument using 20 multiple AO systems, spread in the VLT Nasmyth focal plane, and working in parallel independently of each other as shown in Fig. 11.

Although the complexity of such an instrument may appear insuperable at first sight, it can be greatly relaxed thanks to the tininess of the compensated field required for each independent galaxy. Indeed, as already demonstrated by the instrument GIRAFFE (Hammer et al. 1999), a FoV of only 3×2 arcsec^2 is sufficient to measure the velocity fields of large spirals at $z \leqslant 1$, as well as galaxies with smaller apparent sizes observed at greater redshifts. This is one order of magnitude smaller than the isoplanatic patch in the NIR, so only one unique deformable mirror conjugated to the pupil is required to correct the whole galaxy.

Moreover, we propose a concept where the AO system is miniaturized. Each IFU, lying in the telescope focal plane, will include its proper micro-DM with proper tiny pupil imaging optics. The wavefront sensors also lie a few centimetres apart, in the focal plane; they are located on the guide stars surrounding the galaxy. Translated into length units in the VLT focal plane, an apparent size of 3×2 arcsec^2 covers a physical size of 1.8×1.2 mm^2, and a median distance of 1 arcmin between galaxy and guide stars translates into $\approx$35 mm. These numbers suggest the size of the system that we propose: the adaptive IFU and the wavefront sensors have to be integrated into suitable optomechanical devices, which should not be too wide (typically less than 20 mm) in order not to obstruct the focal plane and allow use of the closest suitable guide stars for wavefront sensing. Such an integration of the subsystems, together with a separation of their functions (the DM and the wavefront sensor become separate, physically independent items), allows us to move those devices into the VLT focal plane just as the positioner OzPoz does with the IFUs used on GIRAFFE (Hammer et al. 1999).

In addition to offering an obvious multiplex advantage, the proposed structure combined with a tomographic wavefront sensing approach allows us to overcome the sky coverage problem. Several guide stars, far out in the isoplanatic patch, are used around each IFU to sense the wavefront. For a 8-m-diameter telescope, it has been shown (Fusco et al. 1999) that three wavefront sensors are sufficient to reconstruct the phase in the pupil for any direction in a FoV of $\approx$2 arcmin diameter and for any turbulence profile; using more wavefront sensors only brings a marginal improvement.

We chose to focus our study on natural guide stars. We believe that using laser guide stars (LGSs), although a very attractive and apparently drastic solution at first sight, could be technically exponentially difficult to implement when dealing with an increasing number of beacons (a minimum of 20 beacons here), while bringing its set of inherent problems such as the cone effect, beacon elongation, superimposition of Rayleigh scattering and beacons, etc. Our approach was then to start the study on natural guide stars, at the risk of doing the study again with LGSs if it is be demonstrated that natural guide stars do not allow us to fulfil the requirements.

We emphasize that the architecture described above corresponds to an open-loop system, since the wavefront sensor does not get any optical feedback from the deformable mirror of the adaptive IFU: this drastically differs from classical closed-loop AO systems. This is of course extremely challenging in terms of AO components. First, the drifts, the linearity, the hysteresis and the calibration of the DM must be kept to a very low error level in order to be able to control it accurately enough in an open-loop system. Secondly, the wavefront sensor must have a high dynamic range in order to provide reliable absolute open-loop measurements, together with a high sensitivity versus flux level. Such a wavefront sensor does not currently exist and needs to be developed, although some similar attempts have been made in the field of a posteriori speckle imaging (Lane et al. 2003). Thirdly, the miniaturization of the components will undoubtedly demand a large technical effort.

On the other hand, an architecture where the optical system is distributed all over the field has the considerable advantage of simplifying the optics. In particular, the field selection functionality becomes here a built-in function, when the number of technical difficulties and the demanding specifications are often underestimated in classical systems. Not only does this critical aspect not exist any more, but also the overall optical throughput of the instrument is boosted, as, at any moment, no dichroic plate is needed to split the light, and because the number of optical surfaces is reduced to its strict minimum. It is important to keep in mind that the efforts put into this instrument have been undertaken to gain not only in spatial resolution, but also in SNR. On this latter particular point, the instrument optical throughput does matter even more than the AO performance, which, in return, will be increased when the wavefront sensor optical transmission is better.

In order to evaluate the system performance in terms of its dimensioning, we ran some numerical simulations. Their presentation and results are the scope of the following section. These simulations assume that we have three natural guide stars per IFU, and a tomographic reconstructor. They are independent of any detailed system configuration, such as the miniaturization of components or the error inherent to open-loop aspects. In this way, they could still apply whatever the technical solution. As an example, a system where the Nasmyth field is optically sliced into sub-fields, themselves sent to independent closed-loop mono-mirror tomographic multi-analysis systems, would lead to the same results.

5 THE FALCON AO SYSTEM: PERFORMANCE

5.1 Introduction

We show in this section the expected performance of an MOAO system like FALCON using atmospheric tomography methods on natural guide stars to reconstruct the on-axis wavefront from any geometry of off-axis measurements. We wrote a Monte Carlo simulation code able to compute the long-exposure PSF corrected by FALCON, for any atmospheric conditions (seeing, outer scale, profile) and for any wavelength. This PSF was then used to compute the Strehl ratio, the FWHM and the ensquared energy in a square aperture of any size.

For all the reasons explained in Section 3.1, we have focused our studies on the evolution of the ensquared energy in an aperture of 0.25×0.25 arcsec^2 (corresponding to 1 kpc for $1 \leqslant z \leqslant 3$). This evolution was studied:

(i) as a function of the size (number of degrees of freedom) and sensitivity (limiting magnitude) of the AO system;

(ii) for two wavelengths, $\lambda = 1.25$ and $\lambda = 1.65$ μm (the central wavelengths of the J and H bands) – as we saw previously, such wavelengths correspond to the observation of the Hα emission line redshifted at $z = 0.9$ and 1.5;

(iii) for three Galactic latitudes, $b \approx -90^\circ, \approx -60^\circ$ and $\approx -30^\circ$, in order to study the gain brought about by atmospheric tomography methods as a function of guide star density, and to estimate the corresponding sky coverage;

© 2007 The Authors. Journal compilation © 2007 RAS, MNRAS **376,** 287–312

Downloaded from https://academic.oup.com/mnras/article/376/1/287/973575 by CNRS - ISTO user on 04 October 2022

(iv) for the median atmospheric conditions of the VLT site (Cerro Paranal, Chile).

A particularly important aspect of this code is the simulation of the tomographic reconstruction, this latter being detailed in Section 5.2.

We did not want to make technical assumptions about the type of DM. For the sake of simplicity, we chose its influence functions to be ZPs. For the same reasons, we assumed that the wavefront sensor measurements directly give the coefficients of the Zernike expansion of the measured wavefront.

5.2 Optimal reconstruction of the on-axis phase from off-axis measurements

We focus here on the reconstruction of the on-axis galaxy phase in the pupil from the off-axis wavefront sensor measurements. The goal is therefore to use natural guide stars for wavefront sensing, which in that case are very likely to be located far outside the isoplanatic angle θ_0, and to determine the best commands to apply to the DM from off-axis measurements, in order to correct the wavefront coming from the direction of the galaxy.

We recall in this section the main points of tomographic reconstruction, as developed by Fusco et al. (2001), himself inspired by Ragazzoni et al. (1999). At a given altitude the phase perturbation is described by its expansion on a modal basis, defined over a disc wider than the pupil and covering any beam imprint of the field [Ragazzoni et al. (1999) call this area the *metapupil*]. Assuming a finite number of turbulent layers, the phase in the whole volume is reduced to one vector, and the game is to express the phase expansion within the pupil, for a given direction, as a matrix product with this vector. Once this relation has been written, the inversion of this linear relation has various solutions, depending on the approach followed by the authors (least-squares, maximum likelihood, etc).

Let us discretize the turbulence profile so that it can be modelled as a finite number N_t of turbulent layers. Assuming a near-field approximation, the resulting phase at a position $\boldsymbol{r}$ in the pupil for a sky direction $\boldsymbol{\alpha}_i$ can therefore be written as the sums of the phase φ_j produced by each turbulent jth layer at the altitude h_j:

$$\Phi(\boldsymbol{r}, \boldsymbol{\alpha}_i) = \sum_{j=1}^{N_\mathrm{t}} \varphi_j(\boldsymbol{r} + h_j \boldsymbol{\alpha}_i). \tag{6}$$

If our system of coordinates is centred on the galaxy (on-axis, $\boldsymbol{\alpha}_i = \mathbf{0}$), then the phase perturbation from the galaxy will be written as

$$\Phi_\mathrm{G}(\boldsymbol{r}, \mathbf{0}) = \sum_{j=1}^{N_\mathrm{t}} \varphi_j(\boldsymbol{r}). \tag{7}$$

Each phase $\Phi(\boldsymbol{r}, \boldsymbol{\alpha}_i)$ can be expanded as a sum of ZPs where we omit the piston term $Z_1(\boldsymbol{r})$:

$$\Phi(\boldsymbol{r}, \boldsymbol{\alpha}_i) = \sum_{k=2}^{\infty} a_{\boldsymbol{\alpha}_i,k} Z_k(\boldsymbol{r}). \tag{8}$$

We assume now that we sense the wavefronts coming from a number N_GS of stars around the galaxy, i.e. we have N_GS wavefront sensors, and that we use the combined measurements of all those wavefront sensors to compute the on-axis phase coming from the galaxy. Moreover, we assume that the wavefront sensor measurements are the coefficients 2 to k_max of the Zernike expansion of the phase, plus some noise. We will now define the *measured phase* as the following quantity:

$$\Phi^m(\boldsymbol{r}, \boldsymbol{\alpha}_i) = \sum_{k=2}^{k_\mathrm{max}} a_{\boldsymbol{\alpha}_i,k} Z_k(\boldsymbol{r}) + n_i(\boldsymbol{r}), \tag{9}$$

where $n_i(\boldsymbol{r})$ is the measurement noise for the wavefront sensor looking at the direction $\boldsymbol{\alpha}_i$, i.e. the propagated noise on the ZPs in the wavefront reconstruction process. We can therefore write

$$n_i(\boldsymbol{r}) = \sum_{k=2}^{k_\mathrm{max}} \boldsymbol{n}_{i,k} Z_k(\boldsymbol{r}). \tag{10}$$

The $\boldsymbol{n}_{i,k}$ coefficients are stored in an $\boldsymbol{n}_i$ vector, which is a random Gaussian vector the statistics of which are given by its covariance matrix $\mathbf{C}_{n,i}$, dependent on the type of wavefront sensor as well as guide star magnitude and readout noise.

We call now $\boldsymbol{\Phi}_{\boldsymbol{\alpha}_i,k_\mathrm{max}}$ the vector storing the coordinates of $\Phi(\boldsymbol{r}, \boldsymbol{\alpha}_i)$ up to the ZP k_max:

$$\boldsymbol{\Phi}_{\boldsymbol{\alpha}_i,k_\mathrm{max}} = \begin{pmatrix} a_{\boldsymbol{\alpha}_i,2} \\ a_{\boldsymbol{\alpha}_i,3} \\ \vdots \\ a_{\boldsymbol{\alpha}_i,k_\mathrm{max}} \end{pmatrix}. \tag{11}$$

This allows us to define the vector $\boldsymbol{\Phi}^m_{\boldsymbol{\alpha}_i}$ storing the coefficients of the phase $\Phi^m(\boldsymbol{r}, \boldsymbol{\alpha}_i)$:

$$\boldsymbol{\Phi}^m_{\boldsymbol{\alpha}_i} = \begin{pmatrix} a_{\boldsymbol{\alpha}_i,2} + \boldsymbol{n}_{i,2} \\ a_{\boldsymbol{\alpha}_i,3} + \boldsymbol{n}_{i,3} \\ \vdots \\ a_{\boldsymbol{\alpha}_i,k_\mathrm{max}} + \boldsymbol{n}_{i,k_\mathrm{max}} \end{pmatrix} = \boldsymbol{\Phi}_{\boldsymbol{\alpha}_i,k_\mathrm{max}} + \boldsymbol{n}_i. \tag{12}$$

Let us consider now the phase perturbation $\varphi_j(\boldsymbol{\rho}_j)$ in the jth turbulent layer. This latter can be expressed also as a sum of ZPs. We call $\boldsymbol{\varphi}_j$ the vector storing the coefficients of this phase up to the index N_j, and we have

$$\boldsymbol{\varphi}_j = \begin{pmatrix} a_{j,2} \\ a_{j,3} \\ \vdots \\ a_{j,N_j} \end{pmatrix}. \tag{13}$$

If we now concatenate all the vectors $\boldsymbol{\varphi}_j$, $j = 1, 2, \ldots, N_\mathrm{t}$, we have the vector $\boldsymbol{\varphi}$ storing the coefficients of the phase in the volume:

$$\boldsymbol{\varphi} = \begin{pmatrix} \boldsymbol{\varphi}_1 \\ \boldsymbol{\varphi}_2 \\ \vdots \\ \boldsymbol{\varphi}_{N_\mathrm{t}} \end{pmatrix}. \tag{14}$$

Ragazzoni et al. (1999), Fusco et al. (2001) and Femenía & Devaney (2003) have shown that there is a linear relation, which we will not detail here, between $\boldsymbol{\Phi}_{\boldsymbol{\alpha}_i,k_\mathrm{max}}$ and $\boldsymbol{\varphi}$. It takes the form

$$\boldsymbol{\Phi}_{\boldsymbol{\alpha}_i,k_\mathrm{max}} = \mathbf{M}^{N_\mathrm{t}}_{\boldsymbol{\alpha}_i} \boldsymbol{\varphi}, \tag{15}$$

where the matrix $\mathbf{M}^{N_\mathrm{t}}_{\boldsymbol{\alpha}_i}$ is called a 'modal projection' matrix, performing the sum of the contributions of each wavefront $\varphi_j(\boldsymbol{\rho}_j)$ on the telescope pupil for a given direction $\boldsymbol{\alpha}_i$. Therefore, if we concatenate all the $\boldsymbol{\Phi}^m_{\boldsymbol{\alpha}_i}$ vectors, $i = 1, 2, \ldots, N_\mathrm{GS}$ into the single vector $\boldsymbol{\Phi}^m$, we can write (Fusco et al. 2001)

$$\boldsymbol{\Phi}^m = \mathbf{M}^{N_\mathrm{t}}_{\boldsymbol{\alpha}} \boldsymbol{\varphi} + \boldsymbol{n}, \tag{16}$$

Downloaded from https://academic.oup.com/mnras/article/376/1/287/973575 by CNRS - ISTO user on 04 October 2022

where $\boldsymbol{n}$ is the concatenation of all the measurement noises $\boldsymbol{n}_i$, $i = 1, 2, \ldots, N_{\rm GS}$, and $\mathbf{M}_{\boldsymbol{\alpha}}^{N_{\rm t}}$ is the generalization to several directions of the matrix $\mathbf{M}_{\boldsymbol{\alpha}_i}^{N_{\rm t}}$.

Let us consider now the on-axis galaxy phase $\Phi_{\rm G}(\boldsymbol{r}, \mathbf{0})$. This latter can also be written as a sum of ZPs:

$$\Phi_{\rm G}(\boldsymbol{r}, \mathbf{0}) = \sum_{k=2}^{\infty} a_{{\rm G},k} Z_k(\boldsymbol{r}). \tag{17}$$

Let $\mathbf{\Phi}_{\rm G}$ be the vector storing all the $a_{{\rm G},k}$ coefficients up to ∞, and $\mathbf{\Phi}_{{\rm G},k_{\max}}$ be the vector storing these coefficients up to the ZP $k_{\max}$. This last vector is also linked to the phase in the volume $\boldsymbol{\varphi}$ by the following relation:

$$\mathbf{\Phi}_{{\rm G},k_{\max}} = \mathbf{M}_{\mathbf{0}}^{N_{\rm t}} \boldsymbol{\varphi}, \tag{18}$$

where $\mathbf{M}_{\mathbf{0}}^{N_{\rm t}}$ is the matrix summing the contributions of each wavefront $\varphi_j(\boldsymbol{\rho}_j)$ on the telescope pupil for the on-axis direction $\boldsymbol{\alpha}_i = \mathbf{0}$. Our goal is to find the best estimate $\hat{\mathbf{\Phi}}_{{\rm G},k_{\max}}$, which will be the vector storing the commands to be applied to the DM, provided that its influence functions are also the ZPs 2 to $k_{\max}$. Therefore the correction phase $\hat{\Phi}_{\rm G}(\boldsymbol{r}, \mathbf{0})$ provided by the DM has the following expression:

$$\hat{\Phi}_{\rm G}(\boldsymbol{r}, \mathbf{0}) = \sum_{k=2}^{k_{\max}} \hat{a}_{{\rm G},k} Z_k(\boldsymbol{r}), \tag{19}$$

and we seek a relation in the form

$$\hat{\mathbf{\Phi}}_{{\rm G},k_{\max}} = \mathbf{W} \mathbf{\Phi}^m, \tag{20}$$

where $\mathbf{W}$ is the reconstruction matrix linking the commands $\hat{\mathbf{\Phi}}_{{\rm G},k_{\max}}$ to the off-axis measurements $\mathbf{\Phi}^m$. Let us define a minimum mean-square error (MMSE) for the reconstruction. In our case we want to minimize the residual variance of the wavefront $\sigma^2_{\varphi,{\rm res}}$:

$$\sigma^2_{\varphi,{\rm res}} = \frac{1}{S} \int_{\mathcal{P}} \left\langle [\Phi_{\rm G}(\boldsymbol{r}) - \hat{\Phi}_{\rm G}(\boldsymbol{r})]^2 \, {\rm d}\boldsymbol{r} \right\rangle \tag{21}$$

$$= \left\langle \left\| \mathbf{\Phi}_{\rm G} - \mathbf{W} \mathbf{\Phi}^m \right\|^2 \right\rangle \tag{22}$$

$$= \sum_{k=2}^{k_{\max}} \left\langle \left(a_{{\rm G},k} - \hat{a}_{{\rm G},k} \right)^2 \right\rangle + \sum_{k=k_{\max}+1}^{\infty} \left\langle a^2_{{\rm G},k} \right\rangle. \tag{23}$$

This residual variance is therefore the sum of two terms:

(i) $\sum_{k=2}^{k_{\max}} \langle (a_{{\rm G},k} - \hat{a}_{{\rm G},k})^2 \rangle$, the reconstruction error due to anisoplanatism and noise propagation; and

(ii) $\sum_{k=k_{\max}+1}^{\infty} \langle a^2_{{\rm G},k} \rangle$, the uncorrected variance due to the finite numbers of ZPs used to correct the wavefront.

We therefore want to minimize $\sum_{k=2}^{k_{\max}} \langle (a_{{\rm G},k} - \hat{a}_{{\rm G},k})^2 \rangle$. The optimal reconstruction matrix satisfying this condition can be written as (Wallner 1983)

$$\mathbf{W}_{\rm opt} = \left\langle \mathbf{\Phi}_{{\rm G},k_{\max}} (\mathbf{\Phi}^{m\rm T}) \right\rangle \left\langle \mathbf{\Phi}^m (\mathbf{\Phi}^{m\rm T}) \right\rangle^{-1}, \tag{24}$$

i.e. this matrix is the product of two matrices: the covariance matrix of the unknowns and of the measurements, and the inverse of the covariance matrix of the measurements. This expression is equivalent to the one obtained by Fusco et al. (2001) with a maximum a posteriori approach.

Using the equations (16) and (18), and as the noise is uncorrelated from the turbulent phase, the equation (24) can be rewritten as

$$\mathbf{W}_{\rm opt} = \mathbf{M}_{\mathbf{0}}^{N_{\rm t}} \mathbf{C}_{\varphi} \left(\mathbf{M}_{\boldsymbol{\alpha}}^{N_{\rm t}} \right)^{\rm T} \left[\mathbf{M}_{\boldsymbol{\alpha}}^{N_{\rm t}} \mathbf{C}_{\varphi} \left(\mathbf{M}_{\boldsymbol{\alpha}}^{N_{\rm t}} \right)^{\rm T} + \mathbf{C}_{\rm n}^{-1} \right]^{-1}. \tag{25}$$

We recognize in this expression the product of two terms.

(i) The matrix $\mathbf{C}_{\varphi} (\mathbf{M}_{\boldsymbol{\alpha}}^{N_{\rm t}})^{\rm T} [\mathbf{M}_{\boldsymbol{\alpha}}^{N_{\rm t}} \mathbf{C}_{\varphi} (\mathbf{M}_{\boldsymbol{\alpha}}^{N_{\rm t}})^{\rm T} + \mathbf{C}_{\rm n}^{-1}]^{-1}$, which gives the best tomographic estimate of the phase in the volume $\boldsymbol{\varphi}$ from off-axis measurements. We find here the same expression as in equation (18) of Fusco et al. (2001).

(ii) The matrix $\mathbf{M}_{\mathbf{0}}^{N_{\rm t}}$: as explained before, it sums the contributions of each wavefront $\varphi_j(\boldsymbol{\rho}_j)$ on the telescope pupil for the on-axis direction $\boldsymbol{\alpha}_i = \mathbf{0}$.

An important point here is the presence of the matrices $\mathbf{C}_{\varphi}$ and $\mathbf{C}_{\rm n}$, introduced by Fusco et al. (2001), which are the generalization for several layers and for several guide stars of the classical turbulence and noise covariance matrices. Thanks to the information contained in these matrices, it is possible to regularize the inversion and increase the FoV where off-axis natural guide stars can be picked off to perform wavefront sensing, as well as to use fainter natural guide stars than in classical least-squares methods. However, these matrices require some a priori knowledge on the noise measurement, and on the turbulence profile.

From a practical point of view, equation (24) shows that 'half' of the optimal matrix can be measured *in situ*: the covariance matrix of the measurements is something that can be obtained from the experiment itself. Only the covariance matrix between real, actual phase and measurements has to be computed.

It should be noted that we used ZPs in our simulation because they are easy to use, useful mathematical tools. However, the current study can be applied to any other modal basis. Further work on the optimal reconstruction matrix in the case of real AO components (Shack–Hartmann or pyramid wavefront sensors, segmented or continuous facesheet DMs) has already been started (Assémat 2004).

5.3 Detailed presentation of the simulation code

The elements of this code are the following.

(i) A mono- or multi-layer turbulent atmosphere. The number of layers, their altitude and the outer scale $\mathcal{L}_0$ as well as the strength of the turbulence in each layer (given by a local r_0) are adjustable. The atmospheric phase screens are simulated using Fourier filtering methods (Shaklan 1989), and take into account the effects of the outer scale $\mathcal{L}_0$ by introducing a proper Von Karman spectrum.

(ii) Any number of natural guide stars, whose positions in the field as well as magnitudes are adjustable.

(iii) Any number of wavefront sensors positioned on the off-axis natural guide stars. The wavefront sensor is supposed to give the Zernike expansion of the phase. Some noise is added to the true Zernike coefficients. The noise is related to the guide star magnitude using the propagation properties in the reconstruction of ZPs. It is then possible to have $N_{\rm GS}$ measurement vectors $\mathbf{\Phi}^m_{\boldsymbol{\alpha}_i}$, which are concatenated in the vector $\mathbf{\Phi}^m$.

(iv) The computation of the reconstruction matrix $\mathbf{W}_{\rm opt}$ from the guide star geometry and magnitudes, the turbulent profile and the number $k_{\max}$ of measured and corrected ZPs.

(v) The computation of the vector $\hat{\mathbf{\Phi}}_{{\rm G},k_{\max}} = \mathbf{W}_{\rm opt} \mathbf{\Phi}^m$ storing the coefficients of the reconstructed on-axis phase on the ZPs 2 to $k_{\max}$.

(vi) A DM with $(k_{\max} - 1)$ actuators, the influence functions of which are also the ZPs 2 to $k_{\max}$, and the commands for which are stored in the vector $\hat{\mathbf{\Phi}}_{{\rm G},k_{\max}}$, allowing us to compute the corrected phase $\hat{\Phi}_{\rm G}(\boldsymbol{r}, \mathbf{0}) = \sum_{k=2}^{k_{\max}} \hat{a}_{{\rm G},k} Z_k(\boldsymbol{r})$.

(vii) The computation of the on-axis residual phase $\Phi_{\rm res}(\boldsymbol{r}, \mathbf{0}) = \Phi_{\rm G}(\boldsymbol{r}) - \hat{\Phi}_{\rm G}(\boldsymbol{r})$.

Downloaded from https://academic.oup.com/mnras/article/376/1/287/973575 by CNRS - ISTO user on 04 October 2022

(viii) The computation of the short-exposure AO-corrected PSFs at different imaging wavelengths.

(ix) The computation of the long-exposure AO-corrected PSFs by averaging the short-exposure AO-corrected PSFs.

We have considered in all these simulations a 8-m telescope (VLT case), the pupil of which was simulated on a discrete grid of 128 × 128 pixels. Assuming Nyquist sampling in the focal plane ($\lambda/2D$), this leads to simulated PSFs covering respectively a field of 4.12 × 4.12 arcsec^2 in the J band and 5.44 × 5.44 arcsec^2 in the H band. Each long-exposure AO-corrected PSF was the average of 100 independent short-exposure PSFs, as we assumed an open-loop system and we did not consider any temporal error.

5.4 Simulation conditions

In this section we give more details about the conditions of the simulations that we performed.

5.4.1 Atmospheric conditions

Let us first deal with atmospheric conditions. We used data from ESO's AO department, who provided us with some statistics about the seeing $\theta_{1/2}$, the isoplanatic angle θ_0 and the coherence time τ_0. We therefore considered some median atmospheric conditions, leading us to the following quantities (all data given for zenith and for a wavelength of 0.5 μm).

(i) A median seeing $\theta_{1/2} = 0.81$ arcsec. This latter is linked to the Fried parameter r_0 by the relation $\theta_{1/2} = 0.976\ \lambda/r_0$. We therefore found a median Fried parameter $r_0 = 12.42$ cm at 0.5 μm for the whole turbulence profile.

(ii) A median isoplanatic angle $\theta_0 = 2.42$ arcsec.

(iii) A median coherence time $\tau_0 = 3.04$ ms.

We therefore used the median seeing and isoplanatic angle to define our turbulence profile, and found that a profile made of three turbulent layers located at altitudes of 0 (ground layer), 1 and 10 km, and with respectively 20, 65 and 15 per cent of the whole turbulence, allowed us to reproduce these atmospheric conditions.

Another important issue is the outer scale $\mathcal{L}_0$, which has a direct influence on the variance of low orders of the turbulence and the FWHM of uncorrected images (Tokovinin 2002). Martin et al. (2000) gave some statistics for this parameter at the Cerro Paranal observatory, and we adopted their median value, i.e. $\mathcal{L}_0 = 24$ m.

5.4.2 AO system parameters

We focus now on the components of the AO system. We considered for each simulation case a tomographic system, with three off-axis wavefront sensors and one DM. As said before, we assumed a correction degree ranging from 0 to 120 ZPs. We assumed that we use wavefront slope sensors (Shack–Hartmann or pyramid), leading to a propagated noise variance on ZPs following a law in $(n+1)^{-2}$ (Rigaut & Gendron 1992).

5.4.3 AO system limiting magnitude

The result of our study depends on the wavefront sensor noise level, and this latter is a function of the photon flux. We assumed that we are in a regime dominated by photon noise. In that case, the noise variance is inversely proportional to the number of photoelectrons per frame (Rigaut & Gendron 1992), $N_{\rm ph}^{-1}$. Hence the noise behaviour of the sensor will entirely be defined versus flux and for any Zernike mode, when the constant of proportionality of the law is given.

The way that we propose to fix this constant of proportionality is to define the flux level that produces a particular noise variance. In order to make this flux level number physically meaningful, we will choose for our noise variance value the one that corresponds to the limiting magnitude of the system. Doing this, setting a limiting magnitude implies a particular noise variance, and consequently defines the complete noise behaviour for any flux level. The usual way of doing it is to derive the wavefront sensor performance (and the limiting magnitude) from the list of wavefront sensor characteristics: detector noise, optical throughput, spectral bandpass, number of lenslets, etc. We think that it is not reasonable to undertake such a study, not only because this would always be possibly technically questionable, out of the scope of this article, but also because a study based on current existing designs might be obsolete in a few years.

Instead, our approach is to consider the wavefront sensor limiting magnitude as the input parameter to our study, not as an output number resulting from a complete modelling of the wavefront sensor. Here, it should be seen as a specification number, when it is a matter of designing the wavefront sensor. The question is then to decide on a value for the noise variance that characterizes the limiting magnitude. The choice is just a matter of definition. In order to give meaningful numbers, we took a criterion that agrees with actual AO users' experience. Practically speaking, the criterion is reached when the user might be discouraged from trying higher magnitudes, considering that the correction only brings marginal improvement. From our experience with the ESO VLT Nasmyth Adaptive Optics System (NAOS), behind this fuzzy rule of thumb is hidden a clear-cut number: we choose a criterion of a noise level value of 250 rad^2 at 0.5 μm. This number really fits with what is actually called the 'limiting magnitude' by the AO community. It corresponds to a magnitude of $R = 17$ (Fusco et al. 2004) on the NAOS system (whose detector on the wavefront sensor has a readout noise equal to 4 e$^-$ rms per pixel). At this magnitude, the NAOS system uses 7 × 7 sub-apertures and controls 42 mirror modes, only 10–15 of them being efficiently compensated.

Now, the choice of the value for the limiting magnitude has to be made. We cannot arbitrarily increase it, and in particular we can set an upper limit, translating into a limiting magnitude the classical laws of photon-noise-limited wavefront sensing which are widely used in the literature. Following Rigaut & Gendron (1992), when the sub-apertures are larger than r_0, the noise variance can be written as

$$\sigma^2 = \frac{2\pi}{n_0 r_0^2}, \tag{26}$$

with n_0 the number of photoelectrons per surface area. Using that formula, if we consider a spectral interval of 0.4 μm, a sampling frequency of 100 Hz and a global optical throughput of 0.5, then the value $\sigma^2 = 250$ rad^2 is attained when $n_0 = 1.63$ photoelectron m^{-2} frame^{-1}, i.e. at a limiting magnitude of $R = 20.0$. This number must be taken as the very upper limit, since this theoretical formula only assumes quantum-noise limitation, excluding any other instrumental effect.

We know that, in the near future, progress in fast-readout detectors may lead to much better results than NAOS. As an example, Low Light Level CCDs (L3CCDs) (Daigle et al. 2004) are extremely good candidates which could bring the noise level below 1 e$^-$ rms per pixel, i.e. increase the limiting magnitude of +1.5 compared with NAOS. However, we have decided to be rather conservative, and we will study in this article two cases of limiting magnitude, $R_{\rm max} = 16$ and 17, that we think are realistic. In that case, one may then wonder how our results shown in Section 5.7 can exhibit corrections up to

Downloaded from https://academic.oup.com/mnras/article/376/1/287/973575 by CNRS - ISTO user on 04 October 2022

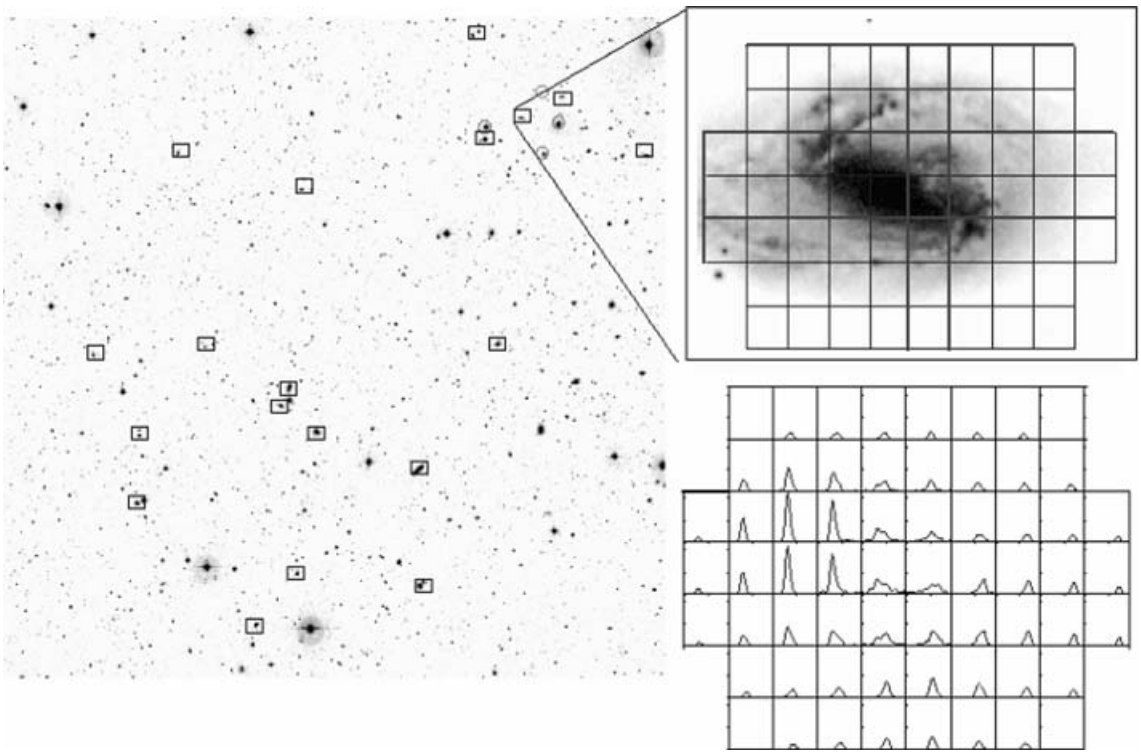

Figure 11. The Falcon concept combines MOAO and tomography: several IFUs (rectangles) are spread over the VLT focal plane. Each IFU is used to perform 3D spectroscopy of one galaxy. Three miniaturized wavefront sensors (circles) measure the wavefront coming from three off-axis natural guide stars located around the galaxy. Their combined signals are used, through a tomographic reconstructor, to command the miniaturized DM in front of the IFU and correct the wavefront. It is therefore possible to recover the velocity field of the galaxy with a better spatial sampling.

120 ZPs, when we noticed that a sensor working at its limiting magnitude – considering our definition – can only efficiently compensate for 10 to 15 Zernike modes (out of 42 effectively handled, and partially corrected). The answer is that the magnitudes of the three guide stars are not simultaneously equal to $R_{\max}$: as shown in Fig. 12, the star surface density increases as a function of the R magnitude by a factor of 2 every 1.5 mag for magnitudes $R > 13$. It means that the median magnitude of a field of stars brighter than $R = R_{\max}$ is equal to $R_{\max} - 1.50$. Then as the signals of the three wavefront sensors are combined together through an optimal reconstructor where both statistics of measurement noise and anisoplanatism are taken into account, thus increasing the final SNR compared with the one that would be given by a single wavefront sensor, this still allows us partially to compensate for high-order modes. As was explained in Section 3.2, such a correction is particularly effective at increasing the ensquared energy of the AO-corrected PSF.

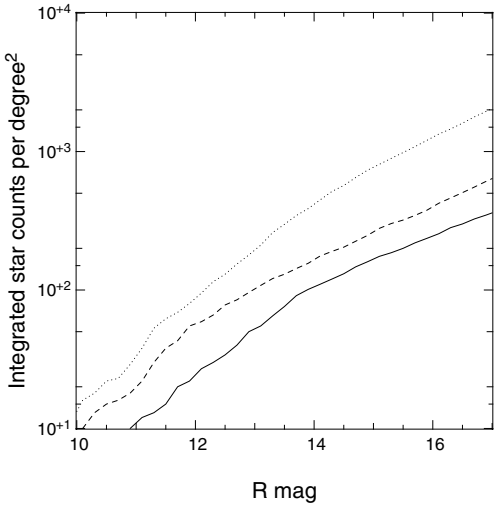

Figure 12. Integrated star counts per square degree in the R band as a function of the R magnitude given by the 'Modèle de Besançon' for three Galactic latitudes: $b \approx -90^\circ$ (full line), $b \approx -60^\circ$ (dashed line) and $b \approx -30^\circ$ (dotted line).

5.4.4 Star density

Let us consider then the three off-axis natural guide stars used to perform off-axis wavefront sensing and on-axis wavefront reconstruction. The angular distances of the first, second and third closest natural guide stars to the central object are directly linked to the Galactic latitude, as the surface density of stars decreases with Galactic latitude (Bahcall & Soneira 1980), and has a direct impact on the performance of the tomographic AO system. In order to have some estimate of the sky coverage of the FALCON AO system, we therefore decided to perform our simulations on three stellar fields, located at the following Galactic coordinates:

(i) $l = 280.^\circ2$, $b = -88.^\circ5$;
(ii) $l = 0.^\circ3$, $b = -61.^\circ4$;
(iii) $l = 44.^\circ5$, $b = -30.^\circ9$.

We used statistics given by the 'Modèle de Besançon' (Robin et al. 2003) to simulate star fields for these three Galactic latitudes. This requires knowledge of the surface densities of stars, which are

© 2007 The Authors. Journal compilation © 2007 RAS, MNRAS **376,** 287–312

Downloaded from https://academic.oup.com/mnras/article/376/1/287/973575 by CNRS - ISTO user on 04 October 2022

Table 2. Number of stars per square degree as a function of the Galactic latitude b and the magnitude $R_{\max}$.

b	$N(R_{\max}=16)$	$N(R_{\max}=17)$	$N(R_{\max}=18)$
-30°	1271	2048	3096
-60°	400	639	946
-90°	246	361	522

shown in Fig. 12, and Table 2 shows the integrated number of stars per square degree for the limiting magnitudes $R_{\max}=16$, 17 and 18. Then, for each field, we chose 100 random positions. For each position, we chose the three closest natural guide stars with a magnitude $R \leqslant R_{\max}$ to perform wavefront sensing, and computed the reconstruction matrix given by equation (25) for each maximal degree of correction. We were then able to reconstruct the on-axis phase from off-axis measurements, and compute the on-axis residual phase, and the long-exposure AO-corrected PSF for different correction orders in the J and H bands.

The quality of the on-axis wavefront reconstruction is directly linked to the geometry of the closest natural guide star used to perform wavefront sensing: anisoplanatism will be increased when the natural guide star is far away from the scientific target. Moreover, as we chose the three closest natural guide stars, it is very likely that these will be faint, meaning significant measurement noise. We therefore give in the next section some analytical formulae for the distances of the first, second and third closest natural guide stars.

5.5 Distances of the closest natural guide stars

Let us call σ_* the surface density of stars, i.e. the number of stars per unit angular surface area on the sky. As an example, the previous section has shown that we have $\sigma_*=246$ stars per square degree for $R_{\max}=16$ and $b\approx-90^\circ$, thus $\sigma_*=0.07$ stars per square arcminute. Therefore, if we call $\mathcal{N}(r)$ the average number of stars in a circle of radius r (in arcminutes), we have $\mathcal{N}(r)=\pi\sigma_* r^2$. As the spatial distribution of stars on the sky follows a uniform probability law, the number of stars in an area of $\pi\sigma_* r^2$ arcmin^2 follows a Poisson law. So, the probability of finding k stars in an area of πr^2 arcmin^2 is equal to

$$P(\xi=k)=\frac{\mathcal{N}^k(r)}{k!}\exp\left[-\mathcal{N}(r)\right]. \tag{27}$$

The probability that there is then *one* star at a distance greater than r is also equal to the probability that there is *no* star in an area equal to $\pi D r^2$ arcmin^2, i.e. $P(\xi=0)=\exp[-\mathcal{N}(r)]=\exp\left(-\pi\sigma_* r^2\right)$. Then, the probability that there is *one* star at a distance $D_1\leqslant r$ is equal to

$$\begin{aligned} P_1(r) &= P(D_1\leqslant r)=1-P(\xi=0)\\ &= 1-\exp\left[-\mathcal{N}(r)\right]\\ &= 1-\exp\left(-\pi\sigma_* r^2\right), \end{aligned} \tag{28}$$

and we recognize the cumulative distribution function (cdf) $P_1(r)$ of the random variable D_1, this latter being the distance of the first closest natural guide star. Then, the probability of having *one* star at a distance between r and $r+\Delta r$ will be equal to the derivative of the cdf of D_1, i.e. its probability density function (pdf) $P_1(r)$, which is equal to

$$\begin{aligned} p_1(r) &= \frac{\mathrm{d}}{\mathrm{d}r}P_1(r)\\ &= 2\pi\sigma_* r\exp\left[-\mathcal{N}(r)\right]\\ &= 2\pi\sigma_* r\exp(-\pi\sigma_* r^2). \end{aligned} \tag{29}$$

As an example, Fig. 13 shows the cdf and the pdf of D_1 for a Galactic latitude $b\approx-90^\circ$ and a limiting magnitude $R_{\max}=16$. Knowing these, it is possible to deduce two interesting quantities. First, the average value of D_1:

$$\begin{aligned} \langle D_1\rangle &= \int_0^\infty r p_1(r)\,\mathrm{d}r\\ &= 2\pi\sigma_*\int_0^\infty r^2\exp(-\pi\sigma_* r^2)\,\mathrm{d}r\\ &= \frac{1}{2\sqrt{\sigma_*}}, \end{aligned} \tag{30}$$

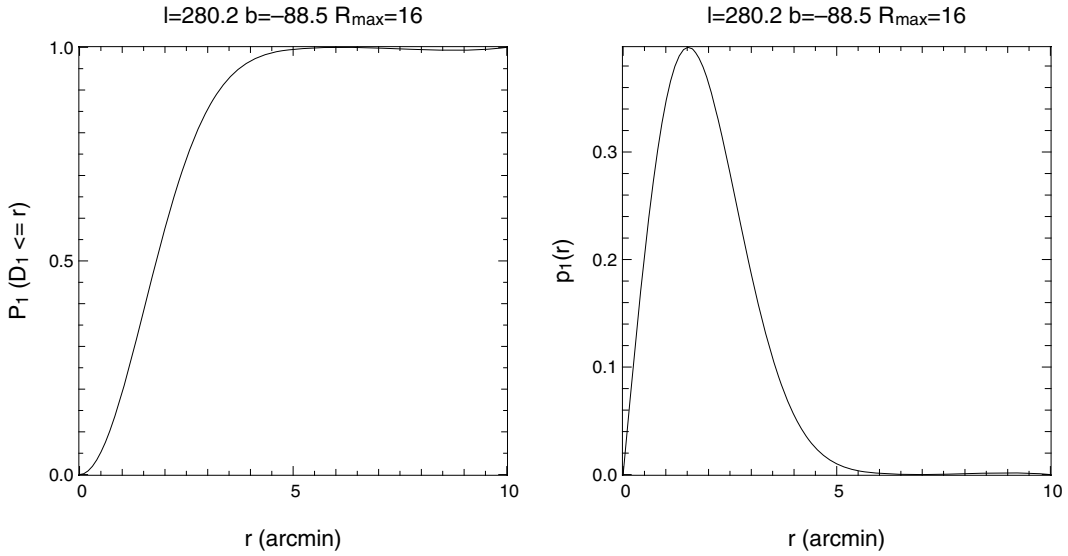

Figure 13. Cumulative distribution function (left) and probability density function (right) of the distance of the first closest natural guide star computed from the stellar density at the Galactic pole ($b\approx-90^\circ$, $R_{\max}=16$) provided by the 'Modèle de Besançon'.

Downloaded from https://academic.oup.com/mnras/article/376/1/287/973575 by CNRS - ISTO user on 04 October 2022

and the most likely value of D_1, that we denote $D_{1,\mathrm{ml}}$, given by the maximum of the pdf $p_1(r)$. The determination of this maximum requires us to compute the derivative of $p_1(r)$, the expression of which is

$$\frac{\mathrm{d}}{\mathrm{d}r}p_1(r) = 2\pi\sigma_* \exp(-\pi\sigma_* r^2)(1 - 2\pi\sigma_* r^2), \tag{31}$$

and which is equal to 0 for

$$D_{1,\mathrm{ml}} = \frac{1}{\sqrt{2\pi\sigma_*}}. \tag{32}$$

Let us focus now on D_2, the distance of the second closest natural guide star. Making the same assumptions as before, the probability of finding two stars at a distance $D_2 \leqslant r$ is equal to

$$\begin{aligned} P_2(r) &= P(D_2 \leqslant r) \\ &= 1 - [P(\xi = 0) + P(\xi = 1)] \\ &= 1 - \exp[-\mathcal{N}(r)][1 + \mathcal{N}(r)] \\ &= 1 - \exp(-\pi\sigma_* r^2)(1 + \pi\sigma_* r^2). \end{aligned} \tag{33}$$

The pdf of D_2 has then the following expression:

$$\begin{aligned} p_2(r) &= 2\pi\sigma_* r\mathcal{N}(r)\exp[-\mathcal{N}(r)] \\ &= 2\pi^2\sigma_*^2 r^3 \exp(-\pi\sigma_* r^2), \end{aligned} \tag{34}$$

and the average value of $\langle D_2\rangle$ can be computed:

$$\begin{aligned} \langle D_2\rangle &= \int_0^\infty r p_2(r)\,\mathrm{d}r \\ &= 2\pi\sigma_* \int_0^\infty r^2\mathcal{N}(r)\exp[-\mathcal{N}(r)] \end{aligned} \tag{35}$$

$$= \frac{3}{4\sqrt{\sigma_*}}. \tag{36}$$

The derivative of $p_2(r)$ is equal to

$$\begin{aligned} \frac{\mathrm{d}}{\mathrm{d}r}p_2(r) &= 2\pi\sigma_*\mathcal{N}(r)\exp[-\mathcal{N}(r)][3 - 2\mathcal{N}(r)] \\ &= 2\pi^2\sigma_*^2 r^2 \exp(-\pi\sigma_* r^2)(3 - 2\pi\sigma_* r^2), \end{aligned} \tag{37}$$

and is equal to 0 for

$$D_{2,\mathrm{ml}} = \sqrt{\frac{3}{2\pi\sigma_*}}. \tag{38}$$

We can now focus on D_3, the distance of the third closest natural guide star. The probability that there are three stars at a distance $D_3 \leqslant r$ is equal to

$$\begin{aligned} P_3(r) &= P(D_3 \leqslant r) = 1 - [P(\xi = 0) + P(\xi = 1) + P(\xi = 2] \\ &= 1 - \exp[-\mathcal{N}(r)]\left[1 + \mathcal{N}(r) + \frac{\mathcal{N}^2(r)}{2}\right] \\ &= 1 - \exp\left(-\pi\sigma_* r^2\right)\left(1 + \pi\sigma_* r^2 + \frac{\pi^2\sigma_*^2 r^4}{2}\right). \end{aligned} \tag{39}$$

The pdf has then the following expression:

$$\begin{aligned} p_3(r) &= \pi\sigma_* r\mathcal{N}^2(r)\exp[-\mathcal{N}(r)] \\ &= \pi^3\sigma_*^3 r^5 \exp(-\pi\sigma_* r^2), \end{aligned} \tag{40}$$

and can be used to compute the average distance $\langle D_3\rangle$:

$$\begin{aligned} \langle D_3\rangle &= \int_0^\infty r p_3(r)\,\mathrm{d}r \\ &= \pi\sigma_* \int_0^\infty r^2\mathcal{N}^2(r)\exp[-\mathcal{N}(r)] \\ &= \frac{15}{16\sqrt{\sigma_*}}. \end{aligned} \tag{41}$$

Table 3. Summary table for the probability density function, and the average and the most likely values of the distance of the closest first, second and third natural guide stars used for tomography as a function of the star surface density σ_*.

	Expression	$\langle D\rangle$	D_{ml}
p_1	$2\pi\sigma_* r \exp\left(-\pi\sigma_* r^2\right)$	$\frac{1}{2\sqrt{\sigma_*}}$	$\sqrt{\frac{1}{2\pi\sigma_*}}$
p_2	$2\pi^2\sigma_*^2 r^3 \exp\left(-\pi\sigma_* r^2\right)$	$\frac{3}{4\sqrt{\sigma_*}}$	$\sqrt{\frac{3}{2\pi\sigma_*}}$
p_3	$\pi^3\sigma_*^3 r^5 \exp\left(-\pi\sigma_* r^2\right)$	$\frac{15}{16\sqrt{\sigma_*}}$	$\sqrt{\frac{5}{2\pi\sigma_*}}$

Table 4. Average and most likely distances of the closest first, second and third natural guide stars as a function of the Galactic latitude and the limiting magnitude. From left to right: the Galactic latitude b, the limiting magnitude $R_{\max}$, the number of stars per square arcmin σ_*, and the average and most likely values of the distances of the off-axis natural guide stars (in arcsec). From stellar densities given by the 'Modèle de Besançon'.

b	$R_{\max}$	σ_*	$\langle D_1\rangle$	$D_{1,\mathrm{ml}}$	$\langle D_2\rangle$	$D_{2,\mathrm{ml}}$	$\langle D_3\rangle$	$D_{3,\mathrm{ml}}$
$-30°$	16	0.35	40	50	70	76	90	94
$-30°$	17	0.57	32	40	55	60	71	75
$-60°$	16	0.11	72	90	124	135	160	169
$-60°$	17	0.17	57	71	98	107	127	133
$-90°$	16	0.07	92	115	158	172	205	215
$-90°$	17	0.10	76	95	130	142	169	177

The first derivative of $p_3(r)$ is equal to

$$\begin{aligned} \frac{\mathrm{d}}{\mathrm{d}r}p_3(r) &= \pi\sigma_*\mathcal{N}^2(r)\exp[-\mathcal{N}(r)][5 - 2\mathcal{N}(r)] \\ &= 2\pi^2\sigma_*^2 r^2 \exp(-\pi\sigma_* r^2)\left[5 - 2\pi\sigma_* r^2\right], \end{aligned} \tag{42}$$

and is equal to 0 for

$$D_{3,\mathrm{ml}} = \sqrt{\frac{5}{2\pi\sigma_*}}. \tag{43}$$

Table 3 summarizes the above results, whereas Table 4 gives some values of distances for the three Galactic latitudes that we studied and for the two cases of limiting magnitude. We can see there that the distances of the closest natural guide stars quickly increase with the Galactic latitude b. As an example, for a limiting magnitude $R_{\max} = 16$, the distance $D_{1,\mathrm{ml}}$ goes from 50 arcsec for $b = -30°$ to 115 arcsec at the Galactic pole. The difference is more significant for the third natural guide star: we have $D_{1,\mathrm{ml}} = 94$ arcsec at $b = -30°$ (which remains usable thanks to tomography), but, at the Galactic pole, the third natural guide star is very likely to be at a distance of more than 3 arcmin! The gain brought by a higher sensitivity then becomes obvious: if fainter natural guide stars (i.e. $R_{\max} = 17$) are used, these distances dramatically decrease. At a Galactic latitude $b = -30°$, the distances of the closest first and third natural guide stars are respectively 10 and 20 arcsec smaller than for $R_{\max} = 16$, and for greater Galactic latitudes ($|b| \geqslant 60°$), these distances are 20 and 35 arcsec smaller. Such differences are not negligible for AO and particularly for the anisoplanatism correction, and show that the improvement of wavefront sensor sensitivities is really mandatory for future systems.

5.6 Sky coverage: definition of a criterion

One of the key issues for AO systems is their sky coverage, i.e. the probability of reaching a certain performance thanks to the

Downloaded from https://academic.oup.com/mnras/article/376/1/287/973575 by CNRS - ISTO user on 04 October 2022

correction provided by AO. For studies of new AO systems, it is very useful to be able to know the variability law of the sky coverage as a function of observing conditions, like the Galactic latitude or the limiting magnitude of off-axis guide stars.

This implies therefore that we need to set the performance we want to reach. As we have seen in Section 3, ensquared energies of 30 per cent in the *J* band and 40 per cent in the *H* band could allow us to reach a sufficient SNR to perform dynamical studies of galaxies located at $z \geqslant 0.9$ with an angular resolution of 0.25 arcsec and a spectral resolution $R = 10\,000$, and a minimum exposure time of 3 h. Such values of absolute ensquared energy can therefore be used as a basis to design the instrument, and we show in the next sections the results that we obtained for this specification. Definitive values of the absolute ensquared energy would, however, require the same simulations for a broader sample of galaxies, which currently are not possible because of the current lack of 3D spectroscopic data for distant galaxies.

5.7 Results

Figs 14 and 15 show the median performance (over 100 natural guide star triplets) of the FALCON AO system, i.e. the evolution of the ensquared energy in an 0.25×0.25 arcsec^2 square aperture and the evolution of the FWHM as a function of the number of corrected ZPs. The panels on the left assume a wavefront sensor with a limiting magnitude $R_{\max} = 16$, the ones on the right a wavefront sensor with the same noise variance as the NAOS visible wavefront sensor ($R_{\max} = 17$). On each figure, three plots are shown: they correspond to Galactic latitudes of 30°, 60° and 90°, and therefore show the performance for 50 per cent of the simulation cases, corresponding to a *sky coverage* of 50 per cent. The specification, i.e. an absolute ensquared energy of 30 or 40 per cent, or a FWHM of 0.25 arcsec, is also drawn on these figures.

The global shape of these curves should be noted. For the ensquared energy curves, we can see that they still significantly

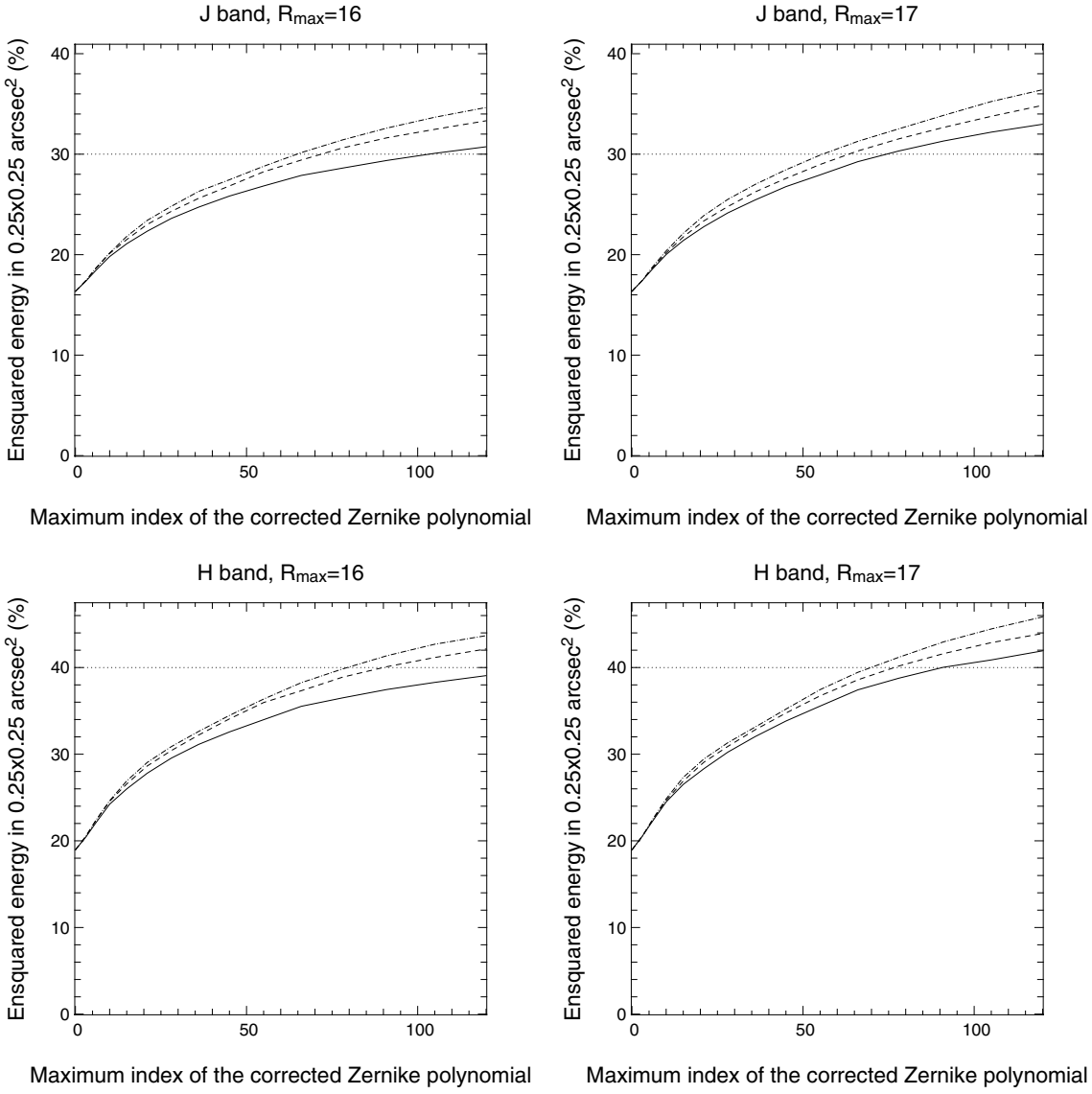

Figure 14. Evolution of the median ensquared energy in a 0.25×0.25 arcsec^2 square aperture for each Galactic latitude b and each limiting magnitude $R_{\max}$ in the *J* and *H* bands, as a function of the number of corrected ZPs. The full line corresponds to the median performance at the Galactic pole, the dashed one to the median performance at $b \approx -60°$, and the dash–dotted one to the median performance at $b \approx -30°$. The dotted horizontal line shows the specification, i.e. 30 per cent in the *J* band and 40 per cent in the *H* band.

Downloaded from https://academic.oup.com/mnras/article/376/1/287/973575 by CNRS - ISTO user on 04 October 2022

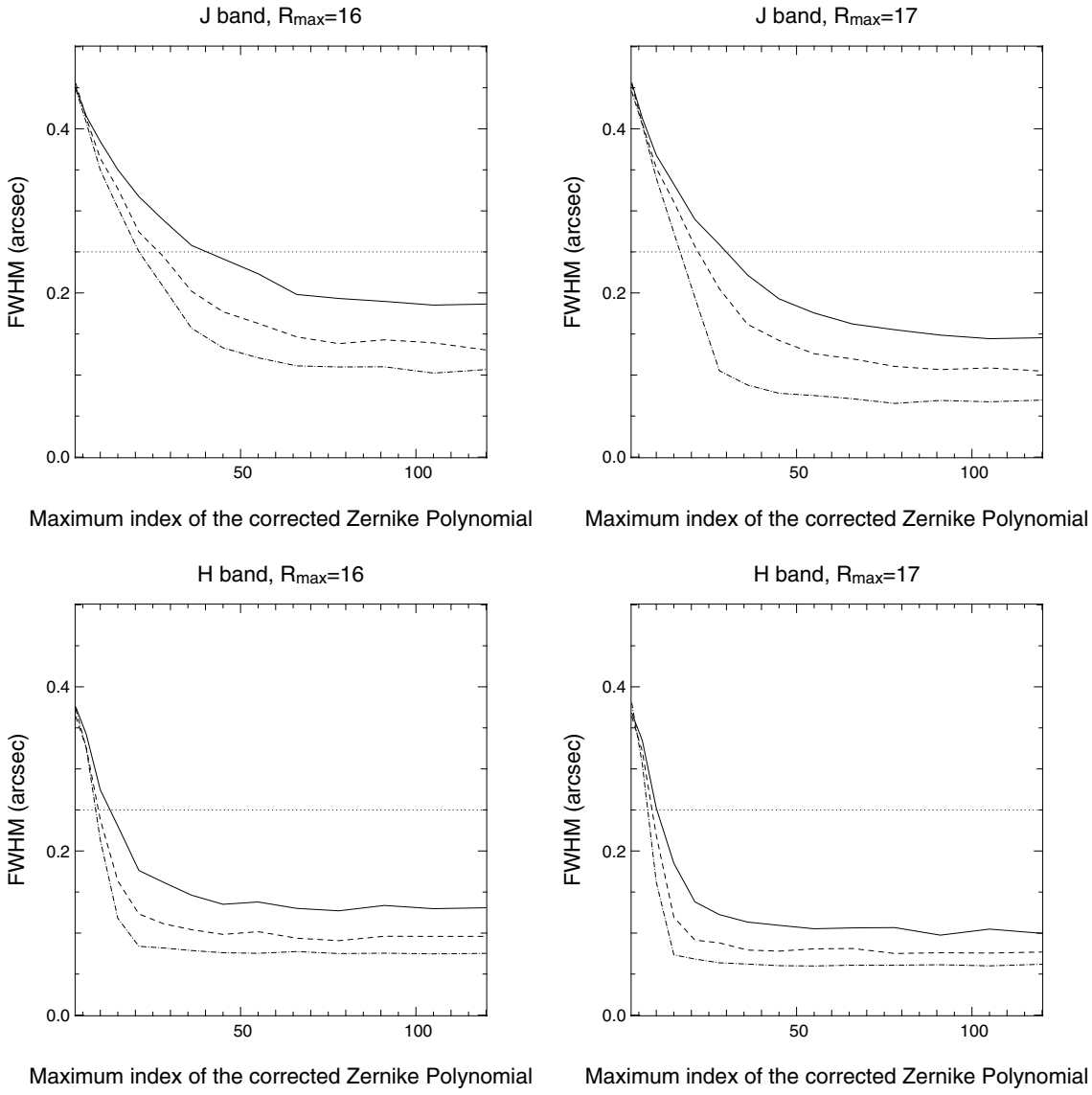

Figure 15. Evolution of the median full width at half-maximum (in arcsec) for each Galactic latitude b and each limiting magnitude $R_{\max}$ in the J and H bands, as a function of the number of corrected ZPs. The full line corresponds to the median performance at the Galactic pole, the dashed one to the median performance at $b \approx -60^{\circ}$, and the dash–dotted one to the median performance at $b \approx -30^{\circ}$. The dotted horizontal line shows the specification, i.e. FWHM = 0.25 arcsec.

increase, even at a high number of corrected modes. However, the FWHM curves quickly saturate to values which are always less than our specification (FWHM = 0.25 arcsec). In fact, as shown in Section 3.2, high-order modes need to be corrected in order to gather the light in the inner regions of the PSF and to improve the ensquared energy. Therefore, to reach our required specifications for the ensquared energy, a non-negligible number of modes must be corrected. For a wavefront sensor with a moderate quality, at least 100 (for the J band) and 120 (in the H band) ZPs must be corrected so that a sky coverage of 50 per cent can be reached for any Galactic latitude b. With a more sensitive wavefront sensor ($R_{\max} = 17$), allowing the use of fainter and closer natural guide stars, the correction order should be only 65 to 85 ZPs to reach the same sky coverage value: the better the wavefront sensor, the lower should be the correction order, as there is a transfer of the phase error between noise and anisoplanatism. The consequence is therefore that a rather large number of actuators would be required, even with the moderate angular resolution required.

These curves show the median values over 100 natural guide star triplets of the expected performance expected thanks to the FALCON AO system. This means that the performance will be better than shown for 50 per cent of cases, and worse for the other 50 per cent. In other words, it means that the performance shown here stands for a sky coverage of 50 per cent.

Immediately, a question arises: whether 50 per cent sky coverage is a sufficient number or not. This seems to be a critical issue, as demonstrated in Fig. 16, where the ensquared energy has been plotted as a function of the number of corrected ZPs and for sky coverages equal to 10, 50 and 90 per cent. We see that for a specification of 40 per cent, the number of corrected modes should be respectively equal to 60, 75 or more than 120! This way of thinking leads therefore to the conclusion that the design of the system is

© 2007 The Authors. Journal compilation © 2007 RAS, MNRAS **376,** 287–312

Downloaded from https://academic.oup.com/mnras/article/376/1/287/973575 by CNRS - ISTO user on 04 October 2022

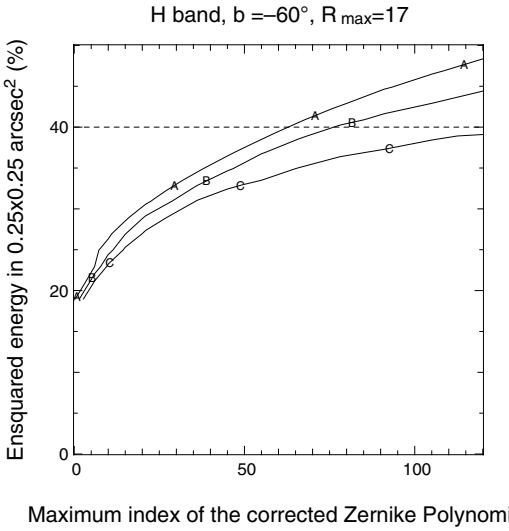

Figure 16. Evolution of the ensquared energy in the *H* band for the field located at $b \approx -60^\circ$ as a function of the corrected number of ZPs, and for a limiting magnitude $R_{\max} = 17$. The line labelled 'A' shows the performance reached for 10 per cent of the simulation cases, line 'B' the performance reached for 50 per cent of the cases, and line 'C' the performance reached for 90 per cent of the cases. The dashed horizontal line shows the specification, i.e. an ensquared energy of 40 per cent.

strongly dependent on the sky coverage. However, this is only partially true, because a sky coverage of 50 per cent does not mean that only half of the objects can be observed whereas the others cannot: it means that 50 per cent of the objects are observable (some of them with an even better quality than expected), and most of the other 50 per cent are observable too, but with a moderate image quality. This latter could, however, be sufficient, as it will be in any case better than the uncompensated seeing-limited image.

As an example, when assuming a median-corrected ensquared energy equal to 40 per cent, 75 ZPs have to be corrected. With such a correction, 95 per cent of the galaxies can be observed with a performance ranging between 36 and 43 per cent. In other words, the dispersion of the ensquared energy provided by AO correction is very low, making the 50 per cent sky coverage a very acceptable performance.

5.8 Conclusion

Thanks to numerical simulations, we have been able to show in this section the expected performance of an MOAO system using atmospheric tomography methods to reconstruct the on-axis wavefront from off-axis measurements performed on natural guide stars, in order to provide simultaneously the 3D spectroscopy of distant galaxies in a 10×10 arcmin^2 FoV. For any Galactic latitude, our results show that an AO system using three very sensitive wavefront sensors (allowing us to measure the wavefront on natural guide stars with a magnitude $R \leqslant 17$) and one DM conjugated to the pupil per scientific target would allow us to reach a spatial resolution better than 0.25 arcsec in the *J* and *H* bands for 95 per cent of the objects, and to achieve an ensquared energy better than 30 per cent in the *J* band and 40 per cent in the *H* band for 50 per cent of the objects. Greater sky coverage (up to 95 per cent) seems to be achievable for slightly lower values of ensquared energy. As explained before, this latter has not been definitely fixed, especially for galaxies with $z \geqslant 1.5$, as further dynamical and photometric data are required to constrain it. However, this requires the correction of a non-negligible number of modes: DMs and wavefront sensors with at least 10×10 actuators and sub-apertures are required to achieve such performance.

From a technological point of view, such a system is very demanding. In particular, the miniaturization of AO components in order to avoid field obstruction is critical, and requires further developments. Some of them have already started: microdeformable mirrors (Zamkotsian et al. 2003) would be very good candidates to be used as wavefront correctors in each IFU. However, the miniaturized and high-dynamic wavefront sensor architecture used in the FALCON AO system remains to be defined.

Therefore, if such an instrumental concept is implemented on the VLT, it will then provide a huge gain in terms of observing time efficiency for the dynamical study of high-redshift galaxies. As an example, recent observations made by the AO-assisted spectrograph SINFONI (Förster Schreiber et al. 2006) have allowed retrieval of the rotation curves of 14 $z \approx 2$ galaxies, with exposure times between 2 and 8 h. However, as SINFONI was used in its natural guide star mode, only two galaxies were observed with a spatial resolution better than atmospheric seeing, the other ones being observed with a spatial resolution of 0.5 arcsec. In other words we can say that SINFONI in natural guide star mode has a sky coverage of $\approx$14 per cent. Moreover, the spectral resolution for these observations was between $R \approx 1900$ and $\approx$4500. These numbers (spatial and spectral resolution, sky coverage) have to be compared with those shown in Sections 3.4 and 5.7, where we can see that the performance of an instrument like FALCON is far beyond the capabilities of SINFONI in its natural guide star mode. The performances of SINFONI in its LGS mode will probably be better in terms of spatial resolution and ensquared energy. However, the fact that very long exposures (see Section 3.4.2) are mandatory to probe the kinematics of distant sources with an 8-m telescope provides an enormous advantage to a multiplex instrument such as FALCON.

6 DISCUSSION

6.1 Comparison with GLAO

The previous section has shown that, thanks to atmospheric tomography, the correction provided by an MOAO system like FALCON allows a huge gain in terms of ensquared energy improvement as well as FWHM reduction, thus allowing us to perform 3D spectroscopy of distant galaxies. However, the use of tomography is quite complex, in particular because it requires a real-time knowledge of the turbulent profile for the computation of the reconstruction matrix.

If we look at the turbulent profile defined in Section 5.4, we can see that 85 per cent of the turbulence is located between altitudes of 0 and 1 km, so very close to the ground. Ground-layer adaptive optics (GLAO) could therefore be used to improve the ensquared energy as well as the angular resolution (Rigaut 2002; Tokovinin 2004). GLAO consists of averaging the measurements from several off-axis guide stars, and is normally very efficient when most of the turbulence is located at or close to the telescope pupil.

The key issue here is to see if GLAO provides a correction as effective as the one provided by tomography, as this would decrease the complexity of the AO system. To answer to this question, we did again the same simulations as described in Section 5. This time, however, instead of using the optimal tomographic reconstruction matrix $\mathbf{W}_{\rm opt}$ to compute the on-axis correction phase, we simply

Downloaded from https://academic.oup.com/mnras/article/376/1/287/973575 by CNRS - ISTO user on 04 October 2022

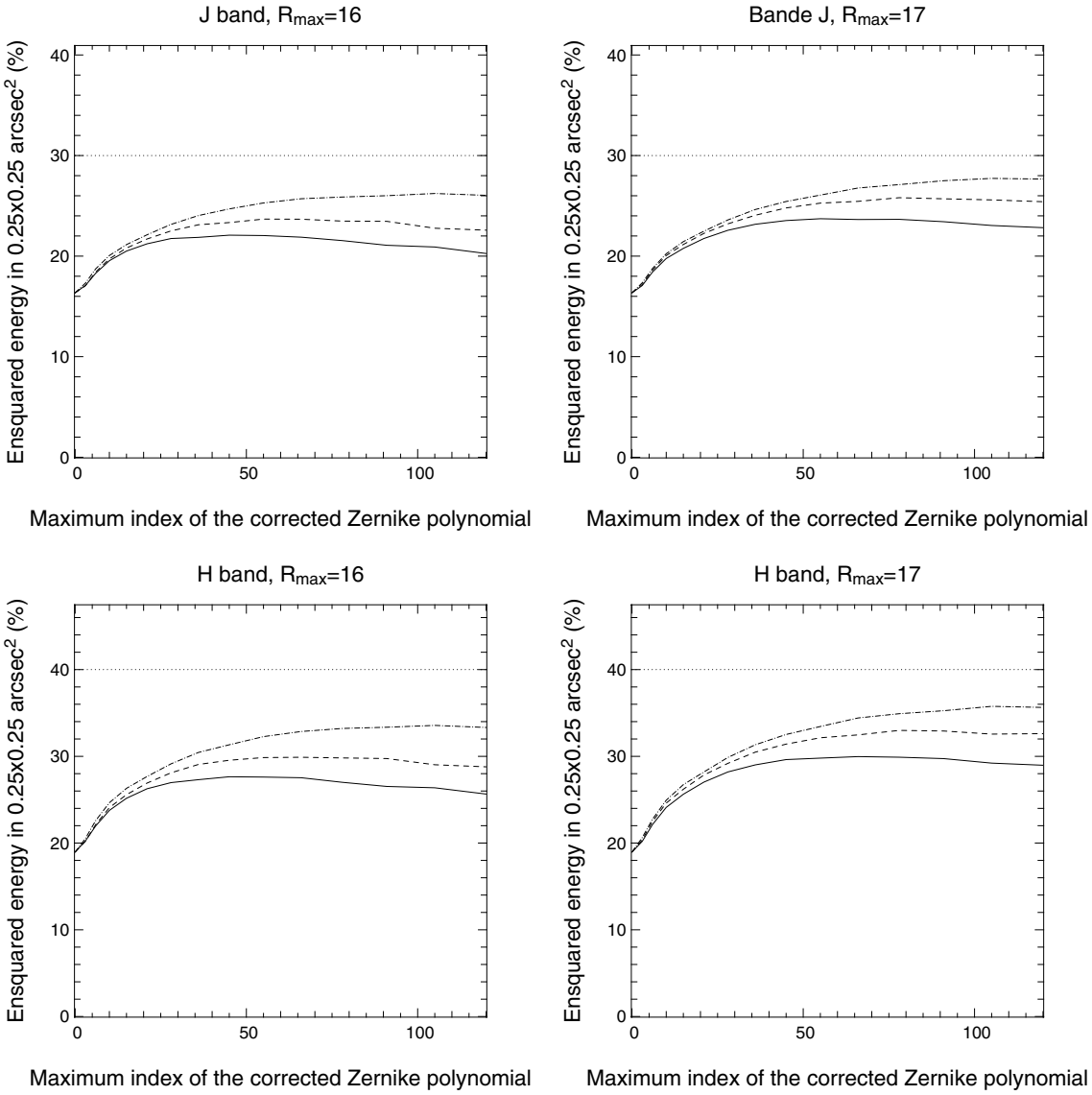

Figure 17. Evolution of the median ensquared energy in a 0.25×0.25 arcsec^2 square aperture for each Galactic latitude b and each limiting magnitude $R_{\max}$ in the J and H bands, as a function of the number of corrected ZPs, in the case of GLAO correction (averaging of off-axis measurements). The full line corresponds to the median performance at the Galactic pole, the dashed one to the median performance at $b \approx -60^\circ$, and the dash–dotted one to the median performance at $b \approx -30^\circ$. The dotted horizontal line shows the specification, i.e. 30 per cent in the J band and 40 per cent in the H band.

calculated an average of the off-axis measurements coming from the three closest guide stars of the science target.

Figs 17 and 18 show the median performance (over 100 natural guide star triplets) of the evolution of the ensquared energy and the FWHM for the three cases of Galactic latitude and the two cases of limiting magnitude already studied, but this time for GLAO correction. For the FWHM, we observe also a saturation of the FWHM, but we can see that even the use of stars with magnitudes $R \leqslant 17$ does not allow us to reach the required angular resolution for all the Galactic latitudes, as the median angular resolution reached at the Galactic pole is equal to 0.30 arcsec. The results are worst for the ensquared energy curves, which show that it is never possible to reach the required ensquared energy values: a GLAO system has a 0 per cent sky coverage for the FALCON specification.

Moreover, a careful examination of the ensquared energy curves shows that their behaviour is quite different from those shown in Fig. 14: contrary to these latter, the curves start to increase, reach an upper limit, and then systematically decrease. This result has to be related to the study of the AO-corrected PSF made in Section 3.2. Indeed, we have shown there that high-order modes must be corrected to bring the energy into the inner parts of the PSF. In GLAO, as an averaging of off-axis measurements is done, there is an important residual anisoplanatism which degrades high-order correction, thus explaining the decrease of the ensquared energy for an important number of corrected modes. This effect is moreover going to be degraded by the noise propagation because of the faint stars used for wavefront sensing.

However, we do not observe such effects when the optimal tomographic reconstruction matrix $\mathbf{W}_{\text{opt}}$ is used. Indeed, the analytical expression of this matrix in equation (25) shows that it uses some a priori information about the turbulence profile as well as the noise, allowing compensation for anisoplanatism and noise.

Downloaded from https://academic.oup.com/mnras/article/376/1/287/973575 by CNRS - ISTO user on 04 October 2022

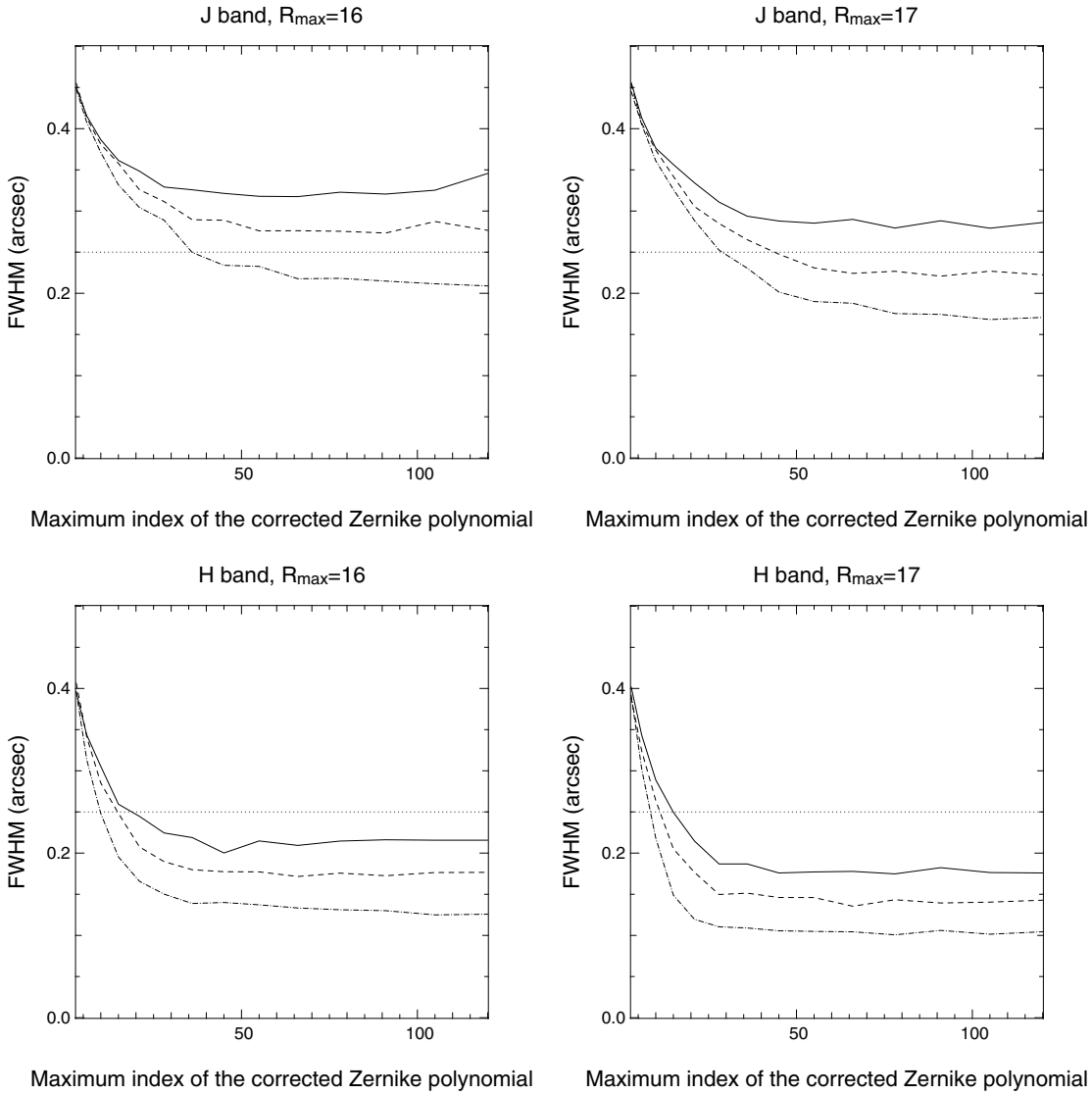

Figure 18. Evolution of the median full width at half-maximum (in arcsec) for each Galactic latitude b and each limiting magnitude $R_{\max}$ in the J and H bands, as a function of the number of corrected ZPs, in the case of GLAO correction (averaging of off-axis measurements). The full line corresponds to the median performance at the Galactic pole, the dashed one to the median performance at $b \approx -60^\circ$, and the dash–dotted one to the median performance at $b \approx -30^\circ$. The dotted horizontal line shows the specification, i.e. FWHM = 0.25 arcsec.

One of the main justifications of GLAO is to have *reduced-seeing-limited* images. Although providing better angular resolution, the corrected PSF is still seeing-limited, meaning that it is not sharpened enough to gather the light into its inner regions and increase the spectroscopic SNR. As a conclusion, we have shown here that even if GLAO seems to be very promising, it is, however, not sufficient to allow us to perform 3D spectroscopy of distant galaxies. Le Louarn & Hubin (2004) have suggested combining GLAO with LGSs, and found that using four LGSs allows an improvement of the ensquared energy over a FoV equal to 1 arcmin. However, this compensated FoV is still one order of magnitude lower than the 10×10 arcmin^2 required. This means that using GLAO with LGSs over the Nasmyth FoV would again require at least one LGS per scientific target, and we have seen that such an architecture dramatically increases the cost of such an instrument. As a conclusion, GLAO is not usable in a system like FALCON, and the combination of MOAO with atmospheric tomography is the best architecture to reach our scientific goals.

6.2 Influence of other parameters

The goal of the results shown in Section 5 was to allow us to give some first-order specifications for the required FALCON AO system, in terms of sky coverage, limiting magnitude and number of actuators. We therefore found that using stars with magnitudes $R \leqslant 17$ would allow us to satisfy our specifications with a sky coverage of at least 50 per cent for any Galactic latitude. However, as we focused only on the spatial aspect of tomographic reconstruction, we made several simplifications before running our simulations, the consequences of which are far from being negligible for the definitive design of the AO system.

First we assumed that we did not have any focal plane obstruction problem, meaning that the physical size of the AO components (the wavefront sensor or the IFUs) would not be a problem. For a real system, it is possible that the size of the optomechanical devices will be too large, implying that the first closest natural guide star to the scientific target will not be usable for wavefront sensing, and that

Downloaded from https://academic.oup.com/mnras/article/376/1/287/973575 by CNRS - ISTO user on 04 October 2022

it will be necessary to use more distant natural guide stars. In fact, equation (28) gives us the expression of the cdf $P_1(D_1 \leqslant r)$ of D_1, the distance of the first closest natural guide star, and its expression is $P_1(D_1 \leqslant r) = 1 - \exp(-\pi\, \sigma_*\, r^2)$. If we assume that all the devices have the same diameter D_B, and that they can work even when they are in contact with each other, then the distance D_1 will indeed be the device diameter D_B, and the function $P_1(D_1 \leqslant r)$ will give us the probability P_N of not being able to use the first closest natural guide star. We therefore find that P_N and D_B are linked by the following relation:

$$D_B = \sqrt{\frac{1}{\pi\sigma_*} \log\left(\frac{1}{1 - P_N}\right)}, \tag{44}$$

σ_* being the number of stars per unit solid angle; the above expression has to be multiplied by the focal plane scale (35 mm arcmin^{-1} for the VLT Nasmyth focus) to give a physical size. As an example, for $b \approx -30^\circ$, we have $\sigma_* = 0.35$ stars per square arcmin ($R_{max} = 16$) or $\sigma_* = 0.57$ stars per square arcmin ($R_{max} = 17$). Then, if we accept losing 50 per cent of the first closest natural guide stars, we find respective diameters D_B of 28 or 22 mm. These numbers will of course be lower if we want to lose fewer stars.

Another critical issue for AO is the temporal error due to time delay, which we did not take into account for our simulations, and which is going to degrade the performance of the AO system, in particular for high wind velocities. Additional simulations taking into account time delay are required to fix the temporal bandwidth of the system. For MCAO systems, Le Roux et al. (2004) have shown that the use of a Kalman filter allows a very good performance to be reached. Such a system therefore needs to be simulated to see if it could be incorporated into the FALCON AO system.

We must also emphasize the fact that we have simulated an open-loop system, where the off-axis wavefront sensors do not get any feedback from the on-axis DM. Moreover, we have assumed in our simulations perfect components with no errors and with instantaneous response. As we work in an open-loop system, the presence of errors like wavefront sensor aliasing or misalignents, DM hysterisis, and more generally non-linearity is going to have some non-negligible consequences on the performance of the AO system. A tolerance analysis is therefore required to quantify the maximum errors that we can accept for each AO subsystem.

Finally, the simulations that we have performed assumed static turbulence conditions, these latter being the median ones at the Cerro Paranal observatory. However, the turbulence is going to change significantly during the long exposure times required by our science objectives. Additional simulations with non-static turbulence conditions are therefore required in order to obtain some definitive realistic instrument performance.

7 CONCLUSIONS

In this paper we have proposed FALCON, a new concept of a multi-object spectrograph for the ESO VLT. Thanks to the combination of AO and atmospheric tomography methods, FALCON will allow 3D spectroscopy of several galaxies located up to $z = 1.5$ with a spatial resolution of 0.25 arcsec and a spectral resolution $R = 10\,000$, in a wide FoV. Such a performance implies the use of MOAO systems, and we have shown that for median Cerro Paranal atmospheric conditions, such systems will allow sky coverages of at least 50 per cent to be reached *for any Galactic latitude*.

In terms of AO components, our simulations have shown that very sensitive wavefront sensors measuring the wavefront from guide stars with magnitudes $R \leqslant 17$ will be required, with 10×10 sub-apertures or actuators. The same number of actuators will be required for the DM in each IFU. Moreover, each DM will require measurements from three off-axis wavefront sensors, as atmospheric tomography methods are needed to improve the sky coverage.

Such an instrumental concept is going to be a real technological challenge, first because of the required miniaturization of the AO components in order to be able to use several AO systems in parallel in the VLT focal plane and to avoid focal plane obstruction: the maximum size of the wavefront sensors and IFUs should not exceed 22 mm. Moreover, as atmospheric tomography is required in order to reach high sky coverages for any Galactic latitude, each independent AO system will work in an open-loop format, meaning that it will use non-classical AO architectures. We have indeed shown that atmospheric tomography is definitely required for the required science objectives, as GLAO will not provide sufficient performance.

Additional studies are required for the final design of the instrument, in particular for the temporal bandwidth of the AO system and the sensitivity to the variation of atmospheric parameters. However, the extrapolation of a concept like FALCON to the next generation of extremely large telescopes is very promising. As an example, for a 42-m telescope with an $F/15$ focal ratio, a 10×10 arcmin^2 field will cover a physical size of $\approx 2 \times 2$ m^2 in the focal plane. Whole-field instrumentation will therefore be impossible to manufacture because of the sizes of the optical components, and an MOAO system will be the best solution for wide-field observations, which will be needed for studies of the very early Universe. Then, the use of an instrument like FALCON, but scaled to an extremely large telescope, will allow us to detail galaxy physics with scales of 400 pc up to $z = 7$, and to understand how galaxies formed since the reionization epoch.

ACKNOWLEDGMENTS

FA is grateful to Véronique Cayatte at Observatoire de Paris-Meudon, and Simon Morris, Richard Myers and Ray Sharples at Durham University for helpful discussions. The authors acknowledge the Institut National des Sciences de l'Univers (INSU) and the ESO Adaptive Optics department for financial support.

REFERENCES

Abraham R. G., van den Bergh S., 2001, Sci, 293, 1273
Abraham R. G., Ellis R. S., Fabian A. C., Tanvir N. R., Glazebrook K., 1999a, MNRAS, 303, 641
Abraham R. G., Merrifield M. R., Ellis R. S., Tanvir N. R., Brinchmann J., 1999b, MNRAS, 308, 569
Assémat F., 2004, PhD thesis, Université Paris VI
Assémat F. et al., 2004, in Gonglewski J. D., Stein K., eds, Proc. SPIE Vol. 5237, Optics in Atmospheric Propagation and Adaptive Systems VI. SPIE, Bellingham, p. 211
Baggett W. E., Baggett S. M., Anderson K. S. J., 1998, AJ, 116, 1626
Bahcall J. N., Soneira R. M., 1980, ApJS, 44, 73
Bouwens R. J., Illingworth G. D., Blakeslee J. P., Broadhurst T. J., Franx M., 2004, ApJ, 611, L1
Bundy K., Fukugita M., Ellis R. S., Kodama T., Conselice C. J., 2004, ApJ, 601, L123
Chassat F., 1989, J. Mod. Opt., 20, 13
Cuby F., 2000, Messenger, 101, 3
Daigle O., Gach J.-L., Guillaume C., Carignan C., Balard P., Boisin O., 2004, in Garnett J. D., Beletic J. W., eds, Proc. SPIE Vol. 5499, Optical and Infrared Detectors for Astronomy. SPIE, Bellingham, p. 219

Downloaded from https://academic.oup.com/mnras/article/376/1/287/973575 by CNRS - ISTO user on 04 October 2022

Dekany R. G., Britton M. C., Gavel D. T., Ellerbroek B. L., Herriot G., Max C. E., Veran J.-P., 2004, in Bonaccini D., Ellerbroek B. L., Ragazzoni R., eds, Proc. SPIE Vol. 5490, Advancements in Adaptive Optics. SPIE, Bellingham, p. 879
Dicke R. H., 1975, ApJ, 198, 605
Dickinson M., Papovich C., Ferguson H. C., Budavári T., 2003, ApJ, 587, 25
Ellerbroek B. L. et al., 2003, in Wizinowich P. L., Bonaccini D., eds, Proc. SPIE Vol. 4839, Adaptive Optical System Technologies II. SPIE, Bellingham, p. 55
Erb D. K., Shapley A. E., Steidel C. C., Pettini M., Adelberger K. L., Hunt M. P., Moorwood A. F. M., Cuby J., 2003, ApJ, 591, 101
Femenía B., Devaney N., 2003, A&A, 404, 1165
Ferguson H. C. et al., 2004, ApJ, 600, L107
Flores H. et al., 1999, ApJ, 517, 148
Flores H., Hammer F., Puech M., Amram P., Balkowski C., 2006, A&A, 455, 107
Förster Schreiber N. M. et al., 2006, ApJ, 645, 1062
Foy R., Labeyrie A., 1985, A&A, 152, L29
Freeman K. C., 1970, ApJ, 160, 811
Fusco T., Conan J.-M., Michau V., Mugnier L. M., Rousset G., 1999, Opt. Lett., 24, 1472
Fusco T., Conan J., Rousset G., Mugnier L. M., Michau V., 2001, J. Opt. Soc. Am. A, 18, 2527
Fusco T. et al., 2004, J. Opt. A, 6, 585
Garrido O., Marcelin M., Amram P., Boulesteix J., 2002, A&A, 387, 821
Garrido O., Marcelin M., Amram P., Boissin O., 2003, A&A, 399, 51
Garrido O., Marcelin M., Amram P., 2004, MNRAS, 349, 225
Garrido O., Marcelin M., Amram P., Balkowski C., Gach J. L., Boulesteix J., 2005, MNRAS, 362, 127
Giavalisco M., 2002, ARA&A, 40, 579
Giavalisco M., Livio M., Bohlin R. C., Macchetto F. D., Stecher T. P., 1996, AJ, 112, 369
Hammer F. et al., 1997, ApJ, 481, 49
Hammer F., Hill V., Cayatte V., 1999, J. Astron. Fran., 60, 19
Hammer F., Sayède F., Gendron E., Fusco T., Burgarella D., Cayatte V., Conan J., 2002, in Bergeron J., Monnet G., eds, Scientific Drivers for ESO Future VLT/VLTI Instrumentation, Springer-Verlag, Dordrecht, p. 139
Hammer F. et al., 2004, in Jabbour G., Rantala J., eds, Proc. SPIE Vol. 5382, Emerging Optoelectronic Applications. SPIE, Bellingham, p. 727
Hammer F., Flores H., Elbaz D., Zheng X. Z., Liang Y. C., Cesarsky C., 2005, A&A, 430, 115
Hanuschik R. W., 2003, A&A, 407, 1157
Hatton S., Devriendt J. E. G., Ninin S., Bouchet F. R., Guiderdoni B., Vibert D., 2003, MNRAS, 343, 75
Johnston D. C., Welsh B. M., 1994, J. Opt. Soc. Am. A, 11, 394
Kennicutt R. C., 1992, ApJ, 388, 310
Labbé I. et al., 2003, AJ, 125, 1107
Lane R. G., Tallon M., Thiébaut E., Clare R. M., 2003, in Wizinowich P. L., Bonaccini D., eds, Proc. SPIE Vol. 4839, Adaptive Optical System Technologies II. SPIE, Bellingham, p. 1142
Le Fèvre O. et al., 2000, MNRAS, 311, 565
Le Louarn M., 2002, MNRAS, 334, 865
Le Louarn M., Hubin N., 2004, MNRAS, 349, 1009
Le Roux B., Conan J.-M., Kulcsár C., Raynaud H.-F., Mugnier L. M., Fusco T., 2004, J. Opt. Soc. Am. A, 21, 1261
Liang Y. C., Hammer F., Flores H., Gruel N., Assémat T., 2004, A&A, 417, 905
Lilly S. et al., 1998, ApJ, 500, 75
Madau P., Ferguson H. C., Dickinson M. E., Giavalisco M., Steidel C. C., Fruchter A., 1996, MNRAS, 283, 1388
Maihara T., Iwamuro F., Yamashita T., Hall D. N. B., Cowie L. L., Tokunaga A. T., Pickles A., 1993, PASP, 105, 940
Mannucci F., Basile F., Poggianti B. M., Cimatti A., Daddi E., Pozzetti L., Vanzi L., 2001, MNRAS, 326, 745
Marchetti E. et al., 2003, in Wizinowich P. L., Bonaccini D., eds, Proc. SPIE Vol. 4839, Adaptive Optical System Technologies II. SPIE, Bellingham, p. 317
Marleau F. R., Simard L., 1998, ApJ, 507, 585
Martin F., Conan R., Tokovinin A., Ziad A., Trinquet H., Borgnino J., Agabi A., Sarazin M., 2000, A&AS, 144, 39
Morris T. J., Berry P., Butterley T., Clark P., Dunlop C. N., Myers R. M., Saunter C. D., Wilson R. W., 2004, in Bonaccini D., Ellerbroek B. L., Ragazzoni R., eds, Proc. SPIE Vol. 5490, Advancements in Adaptive Optics. SPIE, Bellingham, p. 891
Noll R. J., 1976, J. Opt. Soc. Am., 66, 207
Ragazzoni R., Marchetti E., Rigaut F., 1999, A&A, 342, L53
Ragazzoni R., Marchetti E., Valente G., 2000, Nat, 403, 54
Rigaut F., 2002, in Vernet E., Ragazzoni R., Esposito S., Hubin N., eds, ESO Conf. Workshop Proc. Vol. 58, Beyond conventional adaptive optics. ESO, Garching, p. 11
Rigaut F., Gendron E., 1992, A&A, 261, 677
Robin A. C., Reylé C., Derrière S., Picaud S., 2003, A&A, 409, 523
Roddier F., 1999, Adaptive optics in astronomy. Cambridge Univ. Press, Cambridge
Roddier F., Northcott M. J., Graves J. E., McKenna D. L., Roddier D., 1993, J. Opt. Soc. Am. A, 10, 957
Rousselot P., Lidman C., Cuby J.-G., Moreels G., Monnet G., 2000, A&A, 354, 1134
Shaklan S. B., 1989, PhD thesis, Univ. Arizona
Sheth K., Regan M. W., Scoville N. Z., Strubbe L. E., 2003, ApJ, 592, L13
Steidel C. C., Shapley A. E., Pettini M., Adelberger K. L., Erb D. K., Reddy N. A., Hunt M. P., 2004, ApJ, 604, 534
Tallon M., Foy R., 1990, A&A, 235, 549
Tokovinin A., 2002, PASP, 114, 1156
Tokovinin A., 2004, PASP, 116, 941
Tokovinin A., Viard E., 2001, J. Opt. Soc. Am. A, 18, 873
Tokovinin A., Le Louarn M., Viard E., Hubin N., Conan R., 2001, A&A, 378, 710
van den Bergh S., 2002, PASP, 114, 797
Wallner E. P., 1983, J. Opt. Soc. Am., 73, 1771
Zamkotsian F., Camon H., Fabre N., Conedera V., Moreaux G., 2003, in Wizinowich P. L., Bonaccini D., eds, Proc. SPIE Vol. 4839, Adaptive Optical System Technologies II. SPIE, Bellingham, p. 711
Zheng X. Z., Hammer F., Flores H., Assémat F., Pelat D., 2004, A&A, 421, 847
Zheng X. Z., Hammer F., Flores H., Assémat F., Rawat A., 2005, A&A, 435, 507

This paper has been typeset from a TEX/LATEX file prepared by the author.

Downloaded from https://academic.oup.com/mnras/article/376/1/287/973575 by CNRS - ISTO user on 04 October 2022